



**HAL**  
open science

## **Reflectance of Jezero crater floor: 1. Data processing and calibration of the infrared spectrometer (IRS) on super cam**

Clément Royer, T. Fouchet, L. Mandon, Franck Montmessin, F. Poulet, O. Forni, J. R. Johnson, C. Legett, S. Le Mouélic, O. Gasnault, et al.

### ► To cite this version:

Clément Royer, T. Fouchet, L. Mandon, Franck Montmessin, F. Poulet, et al.. Reflectance of Jezero crater floor: 1. Data processing and calibration of the infrared spectrometer (IRS) on super cam. *Journal of Geophysical Research. Planets*, 2023, 128 (1), pp.e2022JE007481. 10.1029/2022JE007481 . insu-03908854

**HAL Id: insu-03908854**

**<https://insu.hal.science/insu-03908854>**

Submitted on 12 Jul 2023

**HAL** is a multi-disciplinary open access archive for the deposit and dissemination of scientific research documents, whether they are published or not. The documents may come from teaching and research institutions in France or abroad, or from public or private research centers.

L'archive ouverte pluridisciplinaire **HAL**, est destinée au dépôt et à la diffusion de documents scientifiques de niveau recherche, publiés ou non, émanant des établissements d'enseignement et de recherche français ou étrangers, des laboratoires publics ou privés.

Copyright

# JGR Planets

## RESEARCH ARTICLE

10.1029/2022JE007481

### Special Section:

The Mars Perseverance Rover  
Jezero Crater Floor Campaign

This article is a companion to Mandon  
et al. (2022), <https://doi.org/10.1029/2022JE007450>.

### Key Points:

- The infrared spectrometer of SuperCam on Perseverance has been successfully flight calibrated using the onboard calibration targets
- Calibration permitted to study the most challenging long wavelengths and thus to discover an absorption band at 2.5  $\mu\text{m}$
- Study of the 2.3 and 2.5  $\mu\text{m}$  absorption bands showed the Séítah unit has variable clay and carbonate mixtures with low carbonate content

### Correspondence to:










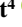







C. Royer,  
[clement.royer@obspm.fr](mailto:clement.royer@obspm.fr)

### Citation:

Royer, C., Fouchet, T., Mandon, L., Montmessin, F., Poulet, F., Forni, O., et al. (2023). Reflectance of Jezero crater floor: 1. Data processing and calibration of the infrared spectrometer (IRS) on SuperCam. *Journal of Geophysical Research: Planets*, 128, e2022JE007481. <https://doi.org/10.1029/2022JE007481>

Received 13 JUL 2022  
Accepted 8 DEC 2022

## Reflectance of Jezero Crater Floor: 1. Data Processing and Calibration of the Infrared Spectrometer (IRS) on SuperCam

C. Royer<sup>1</sup> , T. Fouchet<sup>1</sup> , L. Mandon<sup>1</sup> , F. Montmessin<sup>2</sup> , F. Poulet<sup>3</sup> , O. Forni<sup>4</sup> , J. R. Johnson<sup>5</sup> , C. Legett<sup>5</sup> , S. Le Mouélic<sup>6</sup> , O. Gasnault<sup>4</sup> , C. Quantin-Nataf<sup>7</sup>, P. Beck<sup>8</sup>, E. Dehouck<sup>7</sup> , E. Clavé<sup>9</sup> , A. M. Ollila<sup>10</sup>, C. Pilorget<sup>3</sup>, P. Bernardi<sup>1</sup>, J.-M. Reess<sup>1</sup>, P. Pilleri<sup>4</sup> , A. Brown<sup>11</sup> , R. T. Newell<sup>9</sup> , E. Cloutis<sup>12</sup> , S. Maurice<sup>4</sup>, R. C. Wiens<sup>13</sup> , and The SuperCam Team<sup>14</sup>

<sup>1</sup>LESIA, Observatoire de Paris, Université PSL, CNRS, Sorbonne Université, Université de Paris, Meudon, France, <sup>2</sup>LATMOS, CNRS, Univ. Saint-Quentin-en-Yvelines, Sorbonne University, Guyancourt, France, <sup>3</sup>Institut d'Astrophysique Spatiale, CNRS/Paris-Saclay University, Paris, France, <sup>4</sup>IRAP, CNRS, Université de Toulouse, UPS-OMP, Toulouse, France, <sup>5</sup>Johns Hopkins University Applied Physics Laboratory, Laurel, MD, USA, <sup>6</sup>Nantes Université, Univ Angers, CNRS, UMR 6112, Laboratoire de Planétologie et Géosciences, Nantes, France, <sup>7</sup>Université de Lyon, UCBL, ENSL, CNRS, LGL-TPE, Lyon, France, <sup>8</sup>Université Grenoble-Alpes, CNRS, IPAG, UMR 5274, Grenoble, France, <sup>9</sup>Centre Lasers Intenses et Applications, CNRS, CEA, University of Bordeaux, Bordeaux, France, <sup>10</sup>Los Alamos National Laboratory, Los Alamos, NM, USA, <sup>11</sup>Plancius Research, Severna Park, MD, USA, <sup>12</sup>Department of Geography, University of Winnipeg, Winnipeg, MB, Canada, <sup>13</sup>Purdue University Earth, Atmospheric and Planetary Sciences department, West Lafayette, IN, USA, <sup>14</sup>See Appendix A

**Abstract** The *Perseverance* rover, Mars 2020 mission, landed on the surface of the Jezero crater, on 18 February 2021. This Martian crater is suspected to have hosted a paleolake as evidenced by the numerous detections of aqueously altered phases and thus is a promising candidate for the search for past Martian life. The SuperCam instrument, a collaboration by a consortium of American and European laboratories, plays a leading role in this investigation, thanks to its highly versatile payload providing rapid, synergistic, fine-scale mineralogy, chemistry, and color imaging. After its landing, the first measurements of Martian targets with the infrared spectrometer of SuperCam (IRS) showed new instrumental behaviors that had to be characterized and calibrated to derive unbiased science data. The IRS radiometric response has thus been calibrated using periodic observations of the Aluwhite SuperCam Calibration Target (SCCT). Parasitic effects were understood and mitigated, and the instrumental dark and noise are characterized and modeled. The reflectance calibrated data products, provided periodically on the NASA Planetary Data System, are corrected for the main instrumental features. This radiometric calibration allowed us to study the 2.5  $\mu\text{m}$  absorption band, which has been discovered in the Séítah unit and is associated with phyllosilicates-carbonates mixtures.

**Plain Language Summary** This paper is an instrumental investigation of the infrared spectrometer (IRS) portion of the SuperCam instrument on the Mars Science Laboratory Perseverance rover. Work performed prior to and during flight operations enabled the derivation of a proper instrumental response suitable for calibration of infrared point spectra of rocks and soils observed along the rover traverse. The paper describes development of a full data reduction pipeline in which the radiometric response, sensitivity of the IRS electronic board to temperature, and electromagnetic interference artifacts were removed. A companion paper (Mandon et al., 2022, <https://doi.org/10.1029/2022JE007450>) investigates the IRS data set through Sol 379 in more detail. Here, we specifically explore the 2.5  $\mu\text{m}$  band attributed to carbonates in Séítah unit's phyllosilicate-carbonates mixtures. We found that such mixtures likely have a low carbonate content, which may indicate low amounts of chemical alteration or an alteration by a carbon-poor fluid.

## 1. Introduction

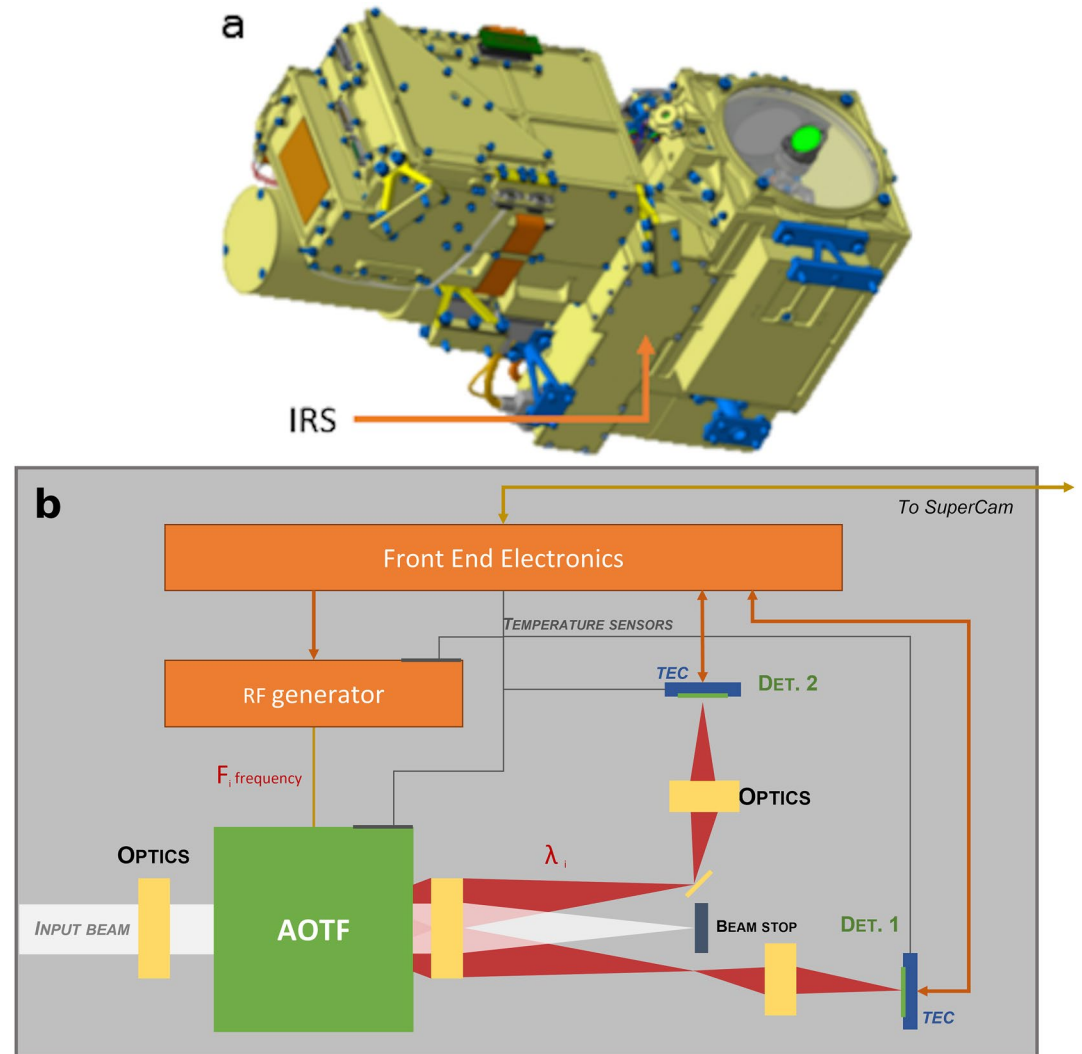
On 18 February 2021, the NASA Mars 2020 *Perseverance* rover landed at the Octavia E. Butler site, on the surface of the 45-km-diameter Jezero crater. This crater, located to the northwest of the Isidis basin, formed during the Noachian era and hosted aqueous activity shaping its landscape (Fassett & Head, 2005; Mangold et al., 2021). The most remarkable feature of Jezero is the presence of the western delta at the mouth of an inlet valley draining fluvial activity in the Nili Planum region (Fassett & Head, 2005; Schon et al., 2012). The crater is known to have hosted a lake, which was inferred as an open basin lake from orbital images (Fassett & Head, 2005;

Gouge et al., 2015), but which also experienced a closed phase as revealed by Perseverance images (Mangold et al., 2021). The total duration of Jezero's lacustrine activity is estimated to be of the order of  $10^6$ – $10^7$  years (Schon et al., 2012), a duration long enough to enable the possibility of habitable environments with appropriate prebiotic chemistry that would have been favorable for the development of microbial life. Evidence for persistent liquid water with appropriate chemistry and organic materials to support habitable environments has been found in Gale crater by the Mars Science Laboratory (MSL; Eigenbrode et al., 2018; Grotzinger et al., 2014).

The Mars 2020 mission follows the logical succession of Martian landed probes, started with Viking 1 and 2 40 years ago and continued by the *Spirit* and *Opportunity* Mars Exploration Rovers and *Curiosity* from MSL. Its main objectives are to determine the geological history of an ancient environment that potentially hosted microbial lifeforms (Farley et al., 2020). The rover shall realize the first step of the Mars Sample Return Program by selecting, characterizing, and collecting rock and regolith samples from the different geologic units within the crater. The SuperCam instrument plays a central role in this investigation. This instrument was designed and built by a consortium of European and American laboratories lead by IRAP (Institut de Recherche en Astrophysique et Planétologie) and LANL (Los Alamos National Laboratory). It consists of a suite of five remote sensing techniques: laser-induced breakdown spectroscopy (LIBS), time-resolved Raman and luminescence spectroscopy (TRR and TRLS), visible–near-infrared spectroscopy (VISIR), remote micro-images, and a microphone. SuperCam is built in two parts: the Body Unit, located in the rover body, and the Mast Unit, located on the top of the rover mast (Maurice et al., 2021; Wiens et al., 2021). SuperCam also features a collection of calibration targets (SuperCam Calibration Target, SCCT) mounted on the rover deck (Cousin et al., 2022; Manrique et al., 2020). The coupling of images and the various spectroscopic techniques makes SuperCam able to study the geology, geochemistry, and mineralogy of the Martian surface, down to the grain scale and with contextual images. The analytical range spans from 2 to 7 m with LIBS and TRR/TRLS and from 2 m to infinity with the passive VISIR spectrometers and images (subject to compensation for atmospheric opacity).

This paper focuses on the near-IR spectrometer (IRS), one of the VISIR spectrometer channels and whose objective is to study the Martian surface in terms of mineralogy and crystal chemistry in a complementary way to LIBS and Raman/TRLS. Through its spectral range (1.3–2.6  $\mu\text{m}$ ), the IRS is sensitive to the signatures of aqueous alteration and the presence of water or -OH in the structure of minerals, as well as some Fe-bearing silicates, such as olivine and pyroxene, which have been detected in the region from orbit (Brown et al., 2020; Horgan et al., 2020; Mandon, 2020). In order to determine the mineralogical composition of rocks and soils observed by the spectrometer, it must be able to detect diagnostic absorption bands of minerals, which can be weak in some cases. The IRS was designed to achieve a signal-to-noise ratio (SNR) of 60 on a spectrum acquired under an average Martian illumination (Fouchet et al., 2022). Pre-launch ground calibration goals were to characterize its radiometric response with an absolute accuracy (continuum level) of at least 20% and a relative precision (from one spectral channel to another) better than 1%. Following these precision objectives, an instrumental transfer function (ITF) was derived to enable calibration of the raw data into reflectance spectra and faithfully reproduce absorption bands a few percent from the mean level. The constraint on the determination of the absolute signal level derived from the needs of spectral modeling and its respect is ensured on the one hand by radiometric calibration and on the other hand by a local illumination model. These performance objectives were achieved during the ground calibration for the parameter space covered Royer et al. (2020). However, limited time during the measurement campaign prevented us from exploring all the instrumental effects to which the IRS could be sensitive, in particular the dependence on variations of the power of the radio frequency (RF) signal supplying the dispersive system (an Acousto-Optic Tunable Filter [AOTF], detailed afterward), which required a thermal regulation of the IR electronic board. This dependence will be discussed in more detail later in the paper. We note that the calibration campaign was carried out during Mars operations, and we retain the same precision objectives as established during the pre-flight calibration campaign.

The paper is organized into four parts. The first part introduces the IRS instrument as well as the general method of characterizing its radiometric response and establishing the data reduction pipeline (Section 2). The second part presents all the results of the instrumental characterizations and the models derived from them (Section 3). The third part details the steps of the data processing pipeline, the calculation of the ITF, and its validation (Section 4). Finally, a fourth part exploits the results of the quantification of the calibration errors to estimate the accuracy of the mineral detections performed during the Crater Floor campaign and gives methods to evaluate the accuracy of spectral parameters based on band depth or slope determination calculations (Section 5).



**Figure 1.** (a) IRS location in the Mast Unit. IRS: Infrared Spectrometer. (b) IRS diagram. AOTF: Acousto-Optic Tunable Filter, Det: detector, TEC: thermo-electrical cooler, RF: radio frequency. Extracted from Royer et al. (2020).

## 2. The IRS Instrument and Its Flight Characterization

### 2.1. Instrument Overview

A thorough description of the IRS and its operating modes can be found in Fouchet et al. (2022). We give here a summary of its main features. The IRS is a standalone near-infrared point spectrometer located in the Mast Unit of SuperCam (Figure 1a). Its most remarkable feature is its compactness (50 mm × 60 mm × 170 mm) allowed by the use of an AOTF that filters input polychromatic light into diffracted monochromatic beams with a high efficiency provided by the acousto-optic diffraction.

In a birefringent crystal excited by an ultrasonic acoustic wave, an incident polychromatic light beam is diffracted by the acoustic waves into two symmetrically separated and cross-polarized monochromatic beams. Thus, four beams emerge from the crystal output: two zero-order beams quasi-aligned, polychromatic, and containing most of the input energy (these are the major source of stray light but they are intercepted by a beam stop) and the two monochromatic diffracted beams, called +1 and −1 both acquired by the detectors of the instrument, respectively, the nominal and the redundant (Figure 1b). The properties of the diffracted beams are directly inherited from the geometry of the crystal and the characteristics of the acoustic waves, themselves generated by a RF electric signal through a piezoelectric transducer. Their central wavelength and intensity are driven by the frequency and

**Table 1**  
*Infrared Spectrometer Main Features*

Spectral range	1.3–2.6 $\mu\text{m}$
	33–68 MHz
Spectral width	26 $\text{cm}^{-1}$
FoV	1.15 mrad
Detector operational temp.	$> -90^\circ\text{C}$
Optical box temperature	$> -35^\circ\text{C}$
AOTF aperture	6 mm $\times$ 6 mm

Note. FoV = field of view.

the power of the RF supply, and their spectral profile is determined by the crystal length and the piezo-electrode shape. The instrument main features are given in Tab. 1.

Several models of the instrument were produced. Of main interest for this study are the IRS Flight Model (FM) and the IRS Flight Spare (FS). Both were integrated with AOTF and other optical and electrical elements produced in the same lots.

The operational temperature of the instrument and its detectors is floored to protect the hardware but is adjusted to the acquisition conditions: the instrument temperature is passively regulated by the ambient air and is kept above  $-35^\circ\text{C}$  by survival heaters; the detector temperature is regulated by a thermoelectric cooling system (TEC) down to  $70^\circ\text{C}$  below the instrument temperature and limited to  $-90^\circ\text{C}$ .

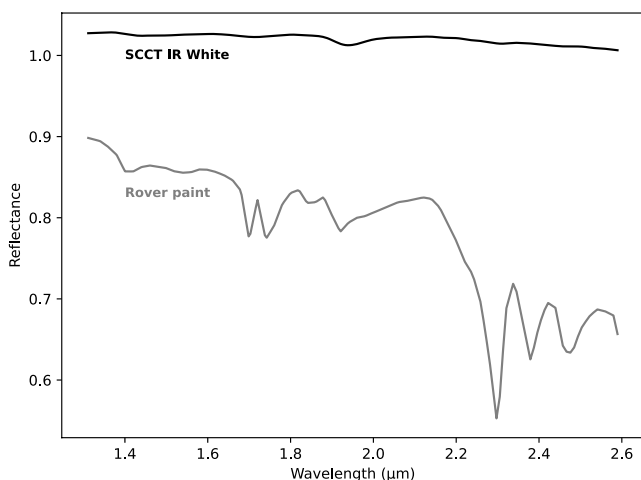
The IRS is operated as follows: during the acquisition of a spectrum, the RF frequency of each spectral channel (256 in full range, adjustable) is set and the signal of the monochromatic beam is integrated by the detector during the given integration time. This component of the data is called “Signal.” Then, the RF supply is turned off to acquire a dark frame containing only the instrument’s thermal background, the detector dark current, and the zero-order stray light, together called “Dark.” This process is repeated for a specified number of accumulations and then for the next channel until the sequence is completed. A typical 256-channels measurement with only one accumulation lasts  $\sim 90$  s. By design, the Signal contains the Dark plus the contribution of the diffracted beam. The latter is retrieved by subtracting Dark from Signal, provided the thermal conditions are the same.

Finally, the IRS relies on the rover’s onboard calibration targets (SCCTs) as a reference signal. In particular, the IR white target provides a near-flat spectrum in the near-IR and an almost Lambertian reflectance. This target has been widely used as a reference for the calibration of the instrument. It is made of AluWhite 98 provided by Avian Technologies (Manrique et al., 2020) and the reference spectrum we used has been measured under an illumination incidence  $i = 0^\circ$  and an emergence  $e = 30^\circ$ , as every other SCCT measurements. By comparison, the rover’s white paint shows strong absorption features, non-suitable as a reference (Figure 2).

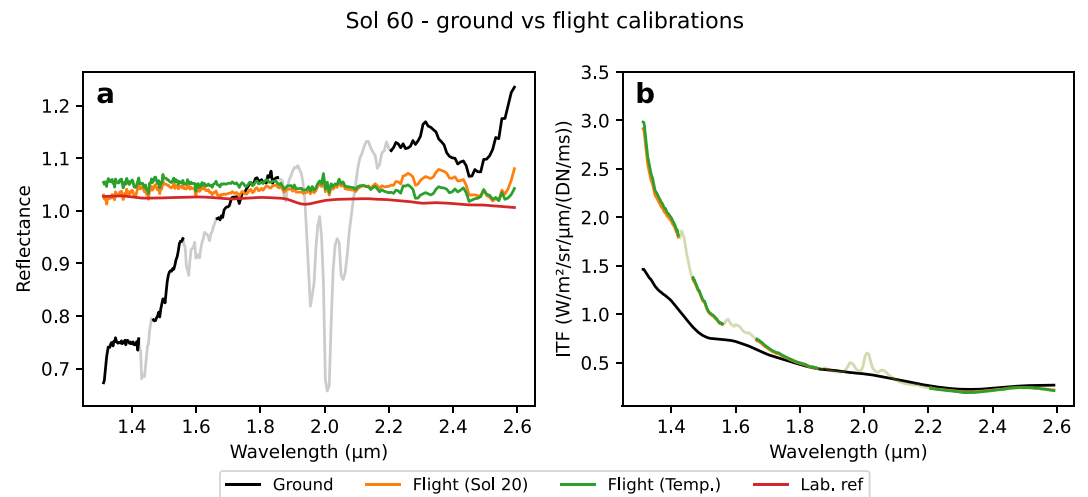
## 2.2. Method

The IRS acquired its first spectrum on Sol 11 (2 March 2021) on the *Máaz* target. These first data exhibited a high SNR and verified the good health of the instrument. They also revealed the necessity to refine our knowledge of the instrument’s response in real Martian conditions, which appeared to be significantly different from what was originally expected (Figure 3). As discussed in Section 4, a first-order flight calibration was derived by observing the IR White SCCT on Sol 20 (first observation of this target) and validated on the next appropriate IR White SCCT observation on Sol 60. It was determined that a sensitivity loss by a factor of up to 2 appeared between the ground calibration and the flight measurements in the low-wavelength part of the spectrum between 1.3 and 1.8  $\mu\text{m}$  (Figure 3b).

In order to understand the behavior of the instrument on Mars and to propose a data reduction procedure, we defined an instrumental characterization campaign in several steps, which evolved as the results were accumulated. From the results of these characterization measurements, we developed a theoretical model to calibrate the acquired data from the raw signal to the reflectance spectra corrected for the instrumental response and its artifacts. The whole data reduction process is implemented in a pipeline fully described in Section 4.



**Figure 2.** Comparison of the reflectance of the SuperCam Calibration Target (SCCT) infrared (IR) White (black line) and the white paint of the rover (gray line). These spectra were acquired in lab, convolved to the infrared spectrometer spectral resolution and resampled.



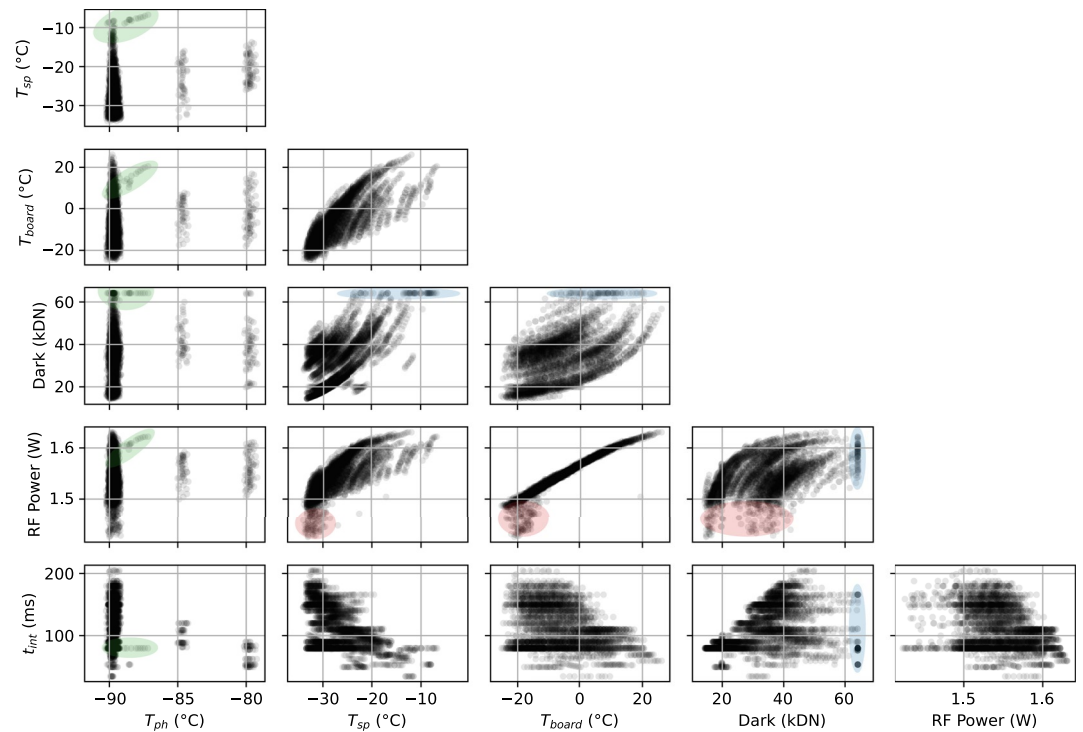
**Figure 3.** (a) Observation of the infrared (IR) White SuperCam Calibration Target (SCCT) on Sol 60, calibrated to reflectance with the ground instrumental transfer function (ITF) (black), the Sol 20 flight ITF (orange), and the temperature calibrated ITF (green). The SCCT lab reflectance spectrum is shown for comparison (red). (b) ITFs derived from the ground calibration (black) from the Sol 20 IR White observation (orange) and temperature calibrated (green). Grayed parts of the spectra correspond to atmospheric absorptions in ground reflectance (panel (a), black line) and flight ITFs (panel (b), orange and green lines). Ground ITF does not contain CO<sub>2</sub> features; therefore, ground calibrated spectra show strong CO<sub>2</sub> lines, in contrast to flight-calibrated ones for which the ITF contains CO<sub>2</sub> features.

### 2.3. Data Set

Here, we present an overview of the data set used in this study. Concerning the measurements made on Mars, we focused on the observations between Sol 11 (first VISIR observation) and Sol 425, which represent a total of 3,363 spectra with their instrumental parameters. Six parameters were mainly studied (Figure 4):

- The temperature of the IRS optical box, called  $T_{sp}$  and measured at the beginning of each spectrum. It was assumed that the temperature of the optical box is homogeneous and representative of the thermal environment of the instrument (which is to be discussed, as we will see in Section 3.1).
- The temperature of the IRS electronic board, containing in particular the RF generator driving the AOTF. This temperature, noted  $T_{board}$ , is strongly correlated to  $T_{sp}$  because the electronic and optical boxes are thermally coupled (Maurice et al., 2021)
- The temperature of the detector,  $T_{ph}$ , regulated by a TEC is selected during the operations, at the lowest at  $-90^{\circ}\text{C}$  and then by steps of  $5^{\circ}\text{C}$ . The dark current of the detector is directly linked to this temperature;
- The Dark, obtained by measuring the signal emitted by the detector when the AOTF is not supplied with RF signal, is the major contributor to the data returned by the instrument. It is highly correlated to the temperatures  $T_{sp}$ ,  $T_{ph}$ , through the dark current and the thermal background, but also to the integration time since it is an integrated quantity.
- The RF signal power is measured throughout the acquisition of the spectra and appears very strongly correlated to the temperature of the electronic board;
- The integration time,  $t_{int}$ , is the duration of the signal's integration. It is set to a constant value for each spectrum with a 1 ms step.

In addition to the flight data, a laboratory measurement campaign on the IRS FS was conducted. These data consist of the observation of a Quartz-Tungsten-Halogen (QTH) lamp stabilized with the IRS thermally regulated inside a climate chamber (a hermetic enclosure at atmospheric pressure whose air is dried and thermally regulated), acquiring both Signal and Dark at various RF power shifts around the nominal profile (Section 3.4).



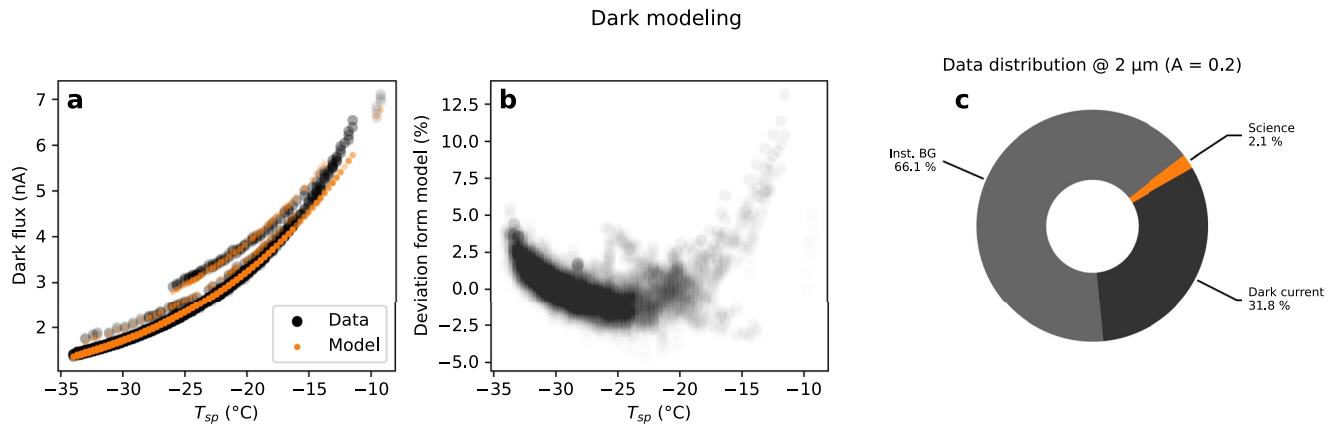
**Figure 4.** Overview of the whole used data set: from Sol 11 to Sol 425, representing 3,363 spectra. The corner plot representation shows the correlation between each studied parameter. Some features are highlighted: the maximum temperature difference between hot and cold faces of the thermoelectric cooling system is 80°C (70°C is kept during the operations for safety); therefore, the temperature became unregulated when  $T_{sp}$  went greater than  $-10^{\circ}\text{C}$  and the set point was  $-90^{\circ}\text{C}$  (green ellipses). The detector, more precisely its analog-to-digital converter, saturates at 65,535 DN. This value has been reached several times during the mission because of high  $T_{sp}$  (blue ellipses). An artifact behaving as radio frequency (RF) power drops occurring randomly during spectra acquisition, called “glitches” appeared several times and was correlated to low  $T_{sp}/T_{board}$  (red ellipses).

### 3. Results of the Characterization Activities

The following sections present the results of the characterization activities performed on the IRS in flight and in lab. These activities consisted of the study of the instrument’s Dark, which depends on the temperature of the detector (dark current) and the temperature of the IRS optical box (thermal background), described in Section 3.1; the study of the noise and the SNR modeled as a sum of independent contributions consisting of the Signal and Dark photon noises, the readout noise and the thermal shot noise of the detector equivalent resistance (Section 3.2); the investigation of the sensitivity of the RF power to the temperature of the electronic board driving the IRS that was discovered during initial mission operations. This first-order thermal effect induces drifts of the RF power injected into the AOTF and thus variations of the crystal transmission. Its characterization required additional laboratory measurements on the IRS FS (Section 3.3). And finally, we characterized the RF power-to-AOTF transmission relation to compensate the temperature-induced power drifts affecting science spectra. This study has been performed in the lab on the FS of the IRS (Section 3.4).

#### 3.1. Dark Characterization and Modeling

A few of the observed discrepancies between ground and flight measurements could be explained by a modification of the Dark behavior of the IRS. Indeed, an instability of the Dark might lead to inconsistent variations of Signal-Dark, since Signal and Dark are not acquired at the same time. Fast Dark variations could lead to residuals when calculating Signal-Dark. As previously explained, the Dark is acquired when the AOTF is not supplied with the RF signal, behaving in this situation as a very efficient optical shutter. The Dark was modeled using flight data, on a narrower thermal range than for the pre-flight campaign, due to operational constraints. The Dark was



**Figure 5.** (a) Dark model fit (orange points) on all acquired data. (b) Deviation from model. (c) The different contributions to the total acquired signal, simulated on an observation with an average albedo of 0.2 at 2  $\mu\text{m}$  and with  $T_{\text{sp}} = -31^\circ\text{C}$ ,  $T_{\text{ph}} = -90^\circ\text{C}$ . Inst. BG: Instrumental background.

modeled using the same model as during the pre-flight calibration (Royer et al., 2020). It relies on two contributions: the thermal background of the instrument ( $i_{\text{BG}}$  related to the temperature of the spectrometer's Optical Box,  $T_{\text{sp}}$ ) and the dark current ( $i_{\text{DC}}$  depending on the temperature of the detector,  $T_{\text{ph}}$ ), where the zero-order stray light was neglected, according to ground characterization results.

- $i_{\text{DC}} = A e^{-\frac{E_a}{kT_{\text{ph}}}}$ . The dark current is fitted with an Arrhenius' law, which gives the best modeling of its behavior. This law models the probability of a system to cross a potential barrier thanks to thermal agitation. It has two parameters: the activation energy  $E_a$  (i.e., the height of the potential barrier), with  $k$  the Boltzmann's constant; and the shock rate,  $A$ , depending on the density of the medium.  $A$  and  $E_a$  are adjusted to data and values are provided below.
- $i_{\text{BG}} = \epsilon_{\text{sp}} \Delta\Omega \int u_\lambda(T_{\text{sp}}) QE d\lambda$ . The thermal background is here modeled as a uniform blackbody emitting light in the whole instrument's field of view, except for the entrance pupil ( $\Delta\Omega$ ), occupied by the optical baffle. The emissivity of the baffle,  $\epsilon_{\text{sp}}$ , is supposed to be independent of the wavelength and is the fitting parameter. The Planck's law,  $u_\lambda(T_{\text{sp}})$ , is integrated over the detector's spectral sensitivity range, represented by its quantum efficiency  $QE$ .

Similarly as for the ground calibration (Royer et al., 2020), the three parameters ( $\epsilon_{\text{sp}}$ ,  $r_0$ ,  $r_1$ ) are fitted on experimental data and the results are given in Figures 5a and 5b, and the fitted parameters are:

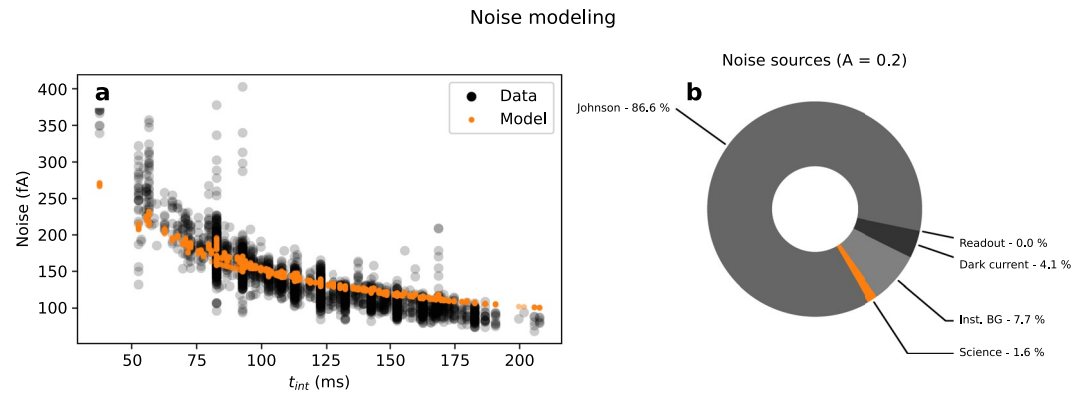
$$\epsilon_{\text{sp}} = 0.9271 \pm 0.0086$$

$$E_a = 0.238 \pm 0.011 \text{ eV}$$

$$A = (1.79 \pm 0.19) \times 10^{-3} \text{ A}$$

This new modeling is very similar to the pre-flight version and more precise: within  $-3\%$  to  $+5\%$ , up to  $+10\%$  at a higher temperature, whereas the ground calibration was about  $\pm 10\%$ , greater than noise probably because of additional uncertainties on the optical baffle temperature value and uniformity. This modeling allows us to assess the relative contribution of dark current, instrumental background and science signal to the total measured signal (Figure 5c). As expected from pre-flight measurements, the flight data set confirms that the Dark component dominates the total signal measured by the IRS, accounting to 98% of the total signal, while the signal from the science target accounts for about 2%. Moreover, the Dark itself is composed of about two thirds of thermal background and one third of dark current in these low-temperature conditions. The thermal background reaches 93% of the total Signal at  $T_{\text{sp}} = -10^\circ\text{C}$  and the science contribution falls down to 0.1%, which illustrates the necessity of operating the instrument in the morning, when the environment and instrument temperatures are the lowest. But as we will show in Section 4.3.1, an instrumental artifact occurs at a low temperature, preventing sensitive measurements from being performed at the lowest possible temperature.





**Figure 6.** (a) Noise model fit (orange points) on all acquired data. (b) Noise variance distribution in Signal-Dark, simulated on an observation with an average albedo of 0.2 at 2  $\mu\text{m}$  and with  $T_{\text{sp}} = -31^\circ\text{C}$ ,  $T_{\text{ph}} = -90^\circ\text{C}$ .

### 3.2. Noise Modeling

The instrument's noise is critical given that it can limit the quality of its data and impact the accuracy of mineral detection/identification. The noise is assumed to have three sources: the photocurrents from diffracted photons and from the Dark are considered as Poisson noise, the variance of which is equal to the average signal:

$$\sigma_{\text{Sci}}^2 = 2 e i_{\text{Sci}} \Delta f \quad (1)$$

$$\sigma_{\text{Dark}}^2 = 2 e i_{\text{Dark}} \Delta f \quad (2)$$

where  $i_{\text{Sci}}$  is the photocurrent from diffracted photons,  $i_{\text{Dark}}$  is the photocurrent from the Dark,  $e$  is the elementary charge, and  $\Delta f = 1/(2 t_{\text{int}})$  is the acquisition bandwidth. The thermal shot noise is generated by the equivalent resistance of the detector (also called Johnson noise). This noise is inherent to any resistive system:

$$\sigma_{\text{John}}^2 = 4 \frac{k T_{\text{ph}}}{R_{\text{load}}} \Delta f \quad (3)$$

with  $k$  the Boltzmann's constant and  $R_{\text{load}}$  the equivalent resistance of the detector (to be adjusted). Finally, the readout noise, whose variance is noted  $\text{RON}^2$ , is a constant representing the uncertainty on the uncertainty of the readout electronics during the integration of the detector electrons. Its value is adjusted in data.

As we knew from the Dark modeling that the signal from the science target is very small compared to the Dark (Section 3.1), the noise characterization has been performed on Dark data only. Its model is fitted by adjusting the values of the equivalent load resistance of the detector ( $R_{\text{load}}$ ) and of the readout noise level (Figure 6a). The fitted values are:

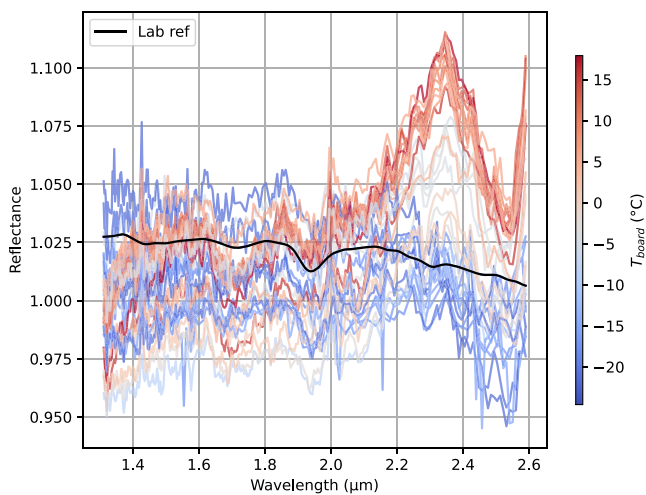
$$R_{\text{load}} = 2.741 \pm 0.028 \text{ M}\Omega \quad (\text{expected } 15.6 \text{ M}\Omega)$$

$$\text{RON} = 4 \times 10^{-4} \pm 1.1 \text{ fA} \quad (\text{expected } 20 \text{ fA})$$

These values are very different from the expected ones, given by the manufacturer of the detector and its readout electronics. The readout noise appears to be poorly constrained and negligible compared to the other values. The equivalent resistance of the detector is much lower, though of the same order. This last parameter represents the lack of a noise source, depending on integration time (contrary to RON) to explain the observed noise, or it highlights an uncertainty on the temperatures used as proxies. Thus, its apparent dominance in the study of the noise distribution means that the major part of noise is from an unknown source (Figure 6b).

### 3.3. Sensitivity to IR Board Temperature

The study of calibrated data revealed a quasi-systematic feature at 2.5–2.6  $\mu\text{m}$  behaving as an absorption band accompanied by a 2.35  $\mu\text{m}$  bump with an intensity reaching up to 10% of mean signal (Figure 7). If not accurately corrected, this would cause a significant limitation in the detection of secondary phase signatures, in particular



**Figure 7.** Infrared (IR) White SuperCam Calibration Target observations from Sol 20 to Sol 354 calibrated to reflectance. The black line is the lab reflectance of the target (greater than 1 because of the AluWhite's slightly non-Lambertian nature. Measured with  $i = 0^\circ$  and  $e = 30^\circ$ ); each color corresponds to the mean temperature of the IR board during the observation. The dispersion of the absolute reflectance is related to the combination of the slightly non-Lambertian nature of the AluWhite and the variability of the solar incidence.

for carbonates. This feature appears to be correlated to the temperature of the IR electronic board, containing the RF generator that supplies the AOTF.

The power delivered by the RF generator follows a similar behavior with respect to the temperature of its electronic board (Figure 8). This parameter is acquired simultaneously with every measurement as a housekeeping (HK) parameter and we find the same  $2.5 \mu\text{m}$  feature as well as another  $1.6 \mu\text{m}$  feature, which is much less present on Signal data. The link between these two observables, the RF power and the integrated Signal, is the instrument's transmission through the AOTF diffraction efficiency. This efficiency depends on the power and the frequency of the RF signal (see Valle, 2017 for further details).

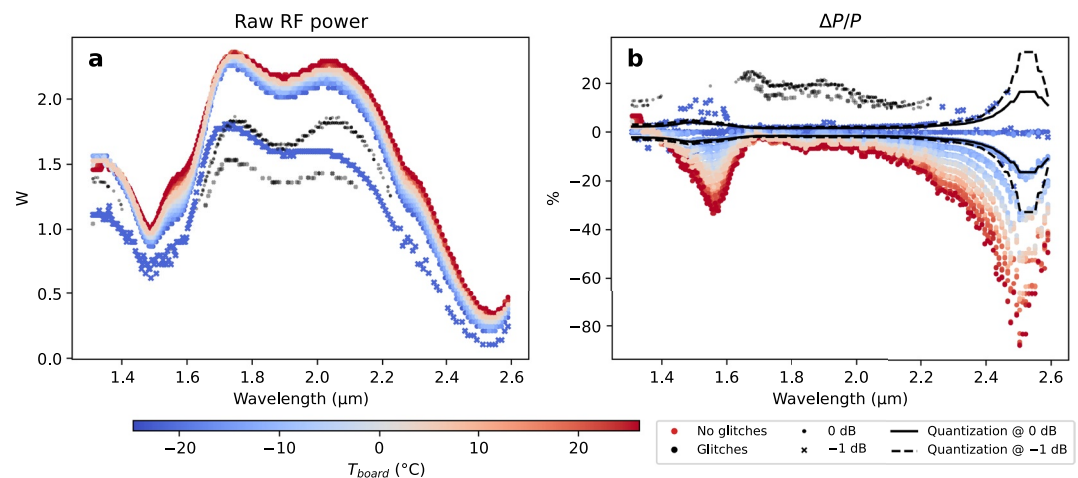
Fortunately, the IR board temperature-to-RF power relation is linear and has been determined with high precision on flight data using two tested RF power attenuations: 0 dB and  $-1$  dB (Figure 9). This linear law is validated on the whole spectral range, and the data present a slight nonlinearity at a high temperature, though lower than the quantization step and not affecting the precision of the calibration.

### 3.4. RF Power to AOTF Transmission Lab Characterization

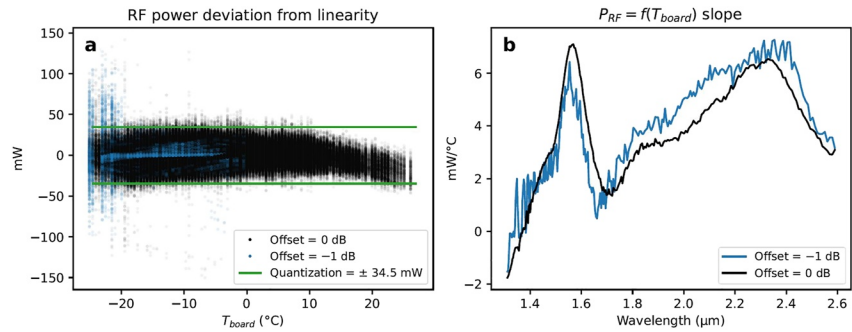
In order to perform a proper calibration of the instrument, the RF power-to-AOTF transmission relation has to be determined, which can be highly nonlinear depending on the AOTF's operating point. Indeed, when operated at high power, an AOTF gets a higher transmission but a nonlinearity appears in the power-to-transmission relation. It varies as  $\sin^2(\alpha \sqrt{P_{RF}})$  with  $\alpha$  depending on the RF frequency and the optical/mechanical properties of the crystal (Valle, 2017).

This law has not been studied during the ground calibration of the IRS (Royer et al., 2020), but was investigated later with lab measurements of the IRS FS in a thermally regulated chamber and illuminated by a QTH lamp. The measurements consisted of the acquisition of the QTH signal at various small RF power deviations around the nominal profile, the instrument being regulated at  $-30^\circ\text{C}$ . The small RF power variations were obtained by tuning the power supply of the RF board, set by default to 20 V and thus called " $20 V_{RF}$ ." Then, the relative transmission

is defined as  $\Delta P/P$ , where  $\Delta P$  is the power deviation and  $P$  is the nominal power. The relative transmission is shown in Figure 8(b) as a function of the infrared board temperature and the attenuation. The plot shows that the power deviation with temperature is greater than the precision of the RF power housekeeping measurement.



**Figure 8.** (a) All radio frequency (RF) power measurements from Sol 11 to Sol 380 as a function of the infrared board temperature (colors) and the attenuation (0 dB = dots,  $-1$  dB = crosses). Black points are glitches, included to show their deviation from the nominal power profile. (b) Relative deviation to Sol 20 power profile. Black lines are the quantization step of the RF power measurement ( $\pm 34.5$  mW). They show that the power deviation with temperature is greater than the precision of the RF power housekeeping measurement.

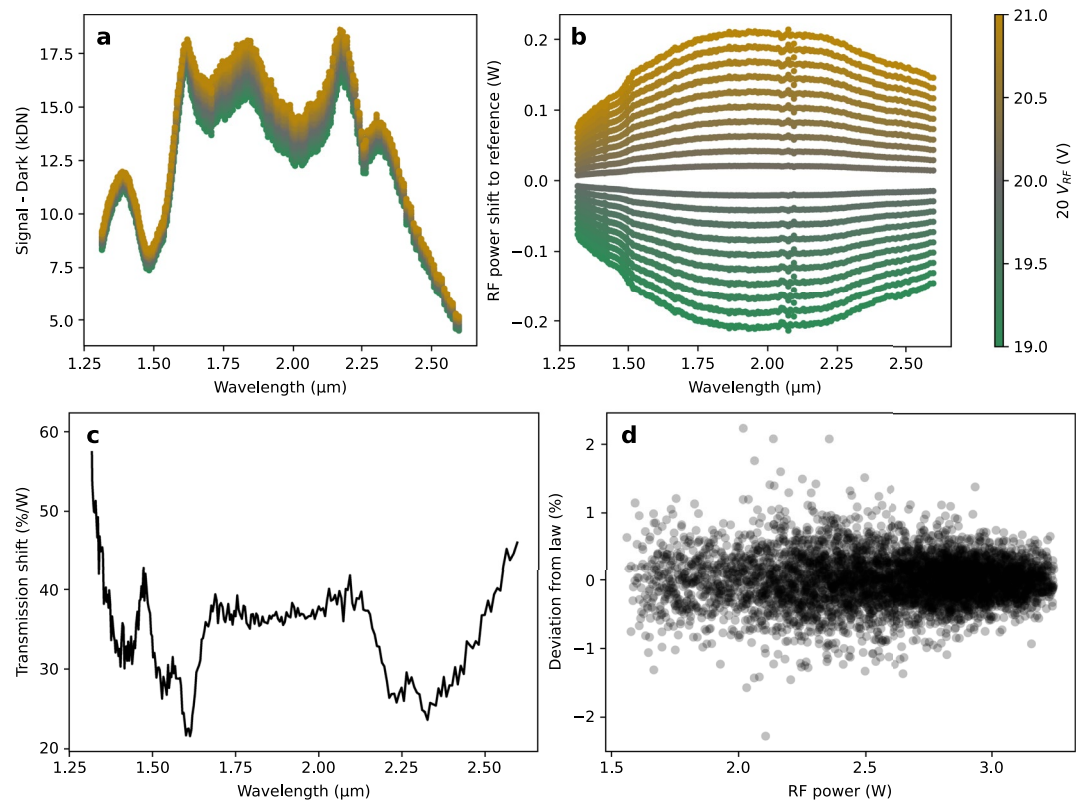


**Figure 9.** (a) Deviation from linearity of every radio frequency (RF) power measurement at the two attenuations. (b) Slope of the linear law representing the sensitivity of the RF power to the temperature.

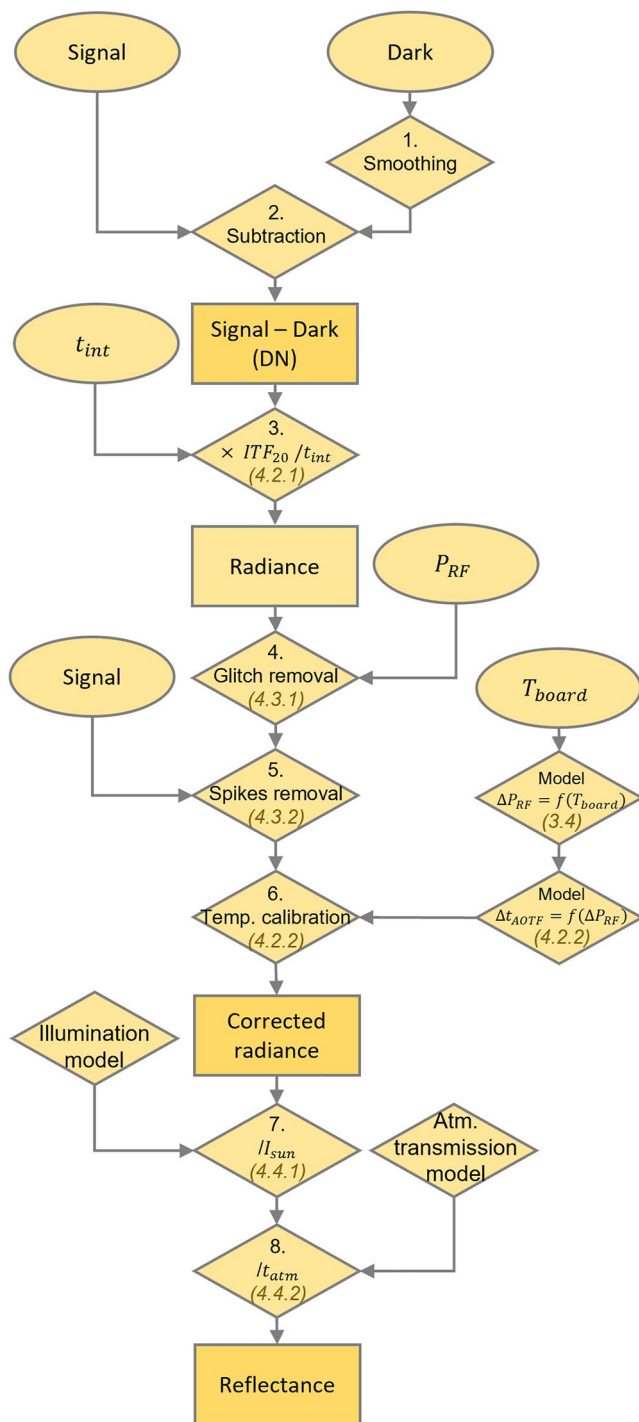
is calculated by dividing the acquired data at a given RF power by the data at the nominal profile (linearity of the instrument). This campaign revealed that the best model describing the power-to-transmission relation is linear on the RF power variation range we observe during the operations on Mars (Figure 10).

#### 4. The IRS Data Processing Pipeline

In this section, we describe the objectives, method, and result of the flight calibration of the IRS. As mentioned in the Introduction, the instrument's response changed significantly between the pre-flight calibration and the first IR White SCCT measurement (Figure 3), which required establishment of a dedicated flight calibration campaign. The objectives of this calibration are to derive an ITF allowing conversion of data into radiance with



**Figure 10.** (a) Signal-Dark measurements as a function of radio frequency (RF) power shift (color corresponds to the variation of the  $20 V_{RF}$  supply). (b) Relative RF power compared to the nominal profile. (c) Slope of the linear law representing the sensitivity of the transmission to the power shift. (d) Deviation from linearity of the transmission measurements.



**Figure 11.** Data reduction pipeline flowchart. Numbers in parenthesis refer to the corresponding section in the paper.

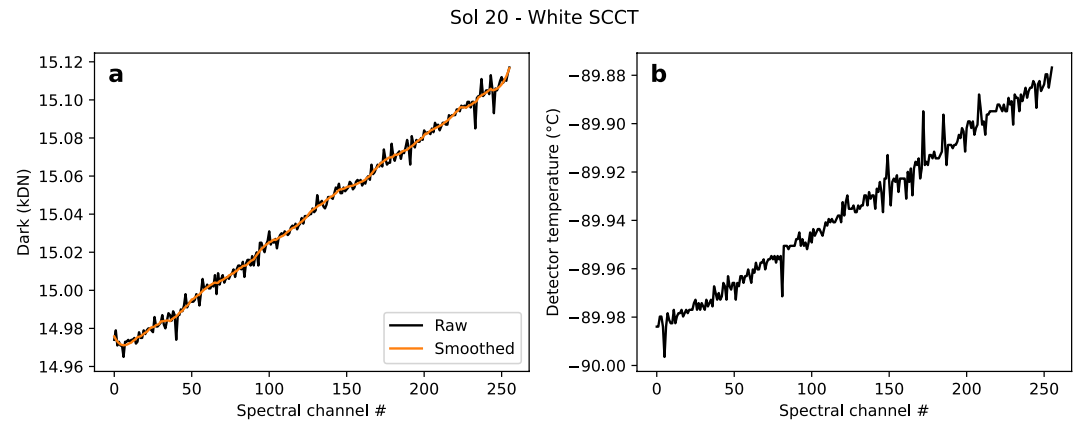
a precision satisfying the science requirement (Royer et al., 2020): 20% in absolute reflectance estimation and 1% in relative. The other objective was to build a data processing pipeline converting the raw digital values into high SNR reflectance data with instrumental artifacts removed.

#### 4.1. The Calibration Pipeline

The IRS calibration is based on an instrument model describing its behavior as a function of integration time and input radiance. This model is linear with both integration time and radiance because of the impossibility to set the observation parameters independently (instrument temperatures and illumination conditions) and has been fitted on IR White measurements (see Section 4.2). The data reduction pipeline is defined as follows (Figure 11):

1. *Dark smoothing.* The IRS Dark is affected by noise as well as readout artifacts called “Spikes” randomly occurring on the whole spectral range (see point 5). Since we know that the Dark is mainly determined by the temperatures of the IR Optical Box and the detector (Section 3.1), its variations should follow their low-frequency trends, and high-frequency noise can be safely removed by a low-pass filter (we use a third-degree Savitzky-Golay filter, Figure 12). Thanks to the fact that the Dark dominates the total integrated Signal, this procedure allows increasing the total SNR by ~40%;
2. *Dark subtraction.* The smoothed Dark is subtracted from the Signal to keep the science contribution only;
3. *Conversion into radiance.* The numerical data are calibrated using the ITF derived on the IR White SCCT measurement acquired on Sol 20 (Equation 4). This zero-order calibration corrects the main instrumental biases, such as the spectral, radiometric, and geometric responses. This process is detailed in Section 4.2.1;
4. *Glitch removal.* Glitches are strong artifacts occurring only on Signal (i.e., only when the AOTF is supplied by RF power) as negative peaks typically affecting only one spectral channel. They are related to the RF power and appear more often at the low temperature (see Section 4.3.1). They are detected on RF power profiles by their strong intensity drop and eliminated by linearly interpolating neighboring nonaffected channels;
5. *Spike removal.* Spikes are also peak-shaped artifacts but they occur on both Signal and Dark, randomly on the whole spectral range and they do not seem related to any instrumental/environmental parameter (Section 4.3.2). Their origin remains unknown at this time. They could be related to an electromagnetic interference/contamination (EMI/EMC) internal to the rover or even to cosmic rays. They are detected on Signal using a 3- $\sigma$  filter (Dark is smoothed as described in point (1) above) and removed by linear interpolation;
6. *Thermal correction.* Final step of the radiometric calibration, radiance spectra are multiplied by a correction vector compensating the instrument's sensitivity to the temperature of its RF electronic board (Section 4.2.2). The resulting corrected radiance is included in PDS data files;

7. *Conversion into reflectance.* Radiance data are converted into reflectance by dividing by a reference radiance, taken as the radiance of an ideal white target illuminated under the same geometry as the observation (solar elevation, Mars-to-Sun distance). We make here the difference between “Martian” targets (i.e., targets on the surface of Mars) and the SCCTs. The Martian targets are assumed to be horizontal because their real illumination geometry is unknown, whereas the SCCTs' solar incidence is very well known. Every target is also assumed to be Lambertian (although this is known to be an approximation). The assumption of a



**Figure 12.** (a) Dark of the Sol 20 AluWhite SuperCam Calibration Target (SCCT) observation. Black line: raw measurement, orange line: smoothed. (b) Evolution of the detector temperature during the spectrum acquisition, correlated to the dark.

horizontal Martian target leads to a local incidence error and a geometric bias, especially for inclined targets (see Section 4.4.1), but it does not affect the shape of the continuum and the position/depth of the absorption features;

8. *Atmospheric correction.* Division of reflectance spectra by an atmospheric transmission reference spectrum, tuned to remove atmospheric spectral features (Section 4.4.2).

## 4.2. Derivation of the Flight Transfer Function

### 4.2.1. Zero-Order Calibration

The “zero-order” calibration is independent of any instrumental or environmental parameter because it relies only on the Sol 20 IR White SCCT observation. The corresponding ITF is calculated through the linear model hypothesis:

$$\text{ITF}_{20} = \frac{I_{\text{Sun},20} \text{Ref}_W}{\text{DN}_{20} / t_{\text{int}20}} \quad (4)$$

where  $I_{\text{Sun},20}$  is the solar radiance reflected by an ideal white Lambertian surface at Sol 20 (see Section 4.4.1),  $\text{Ref}_W$  is the lab reflectance of the IR White target,  $\text{DN}_{20}$  is the Signal-Dark measurement on the IR White SCCT, and  $t_{\text{int}20}$  the corresponding integration time. The unit of the ITF is thus the  $\text{W}/\text{m}^2/\text{sr}/\mu\text{m}/(\text{DN}/\text{ms})$ .

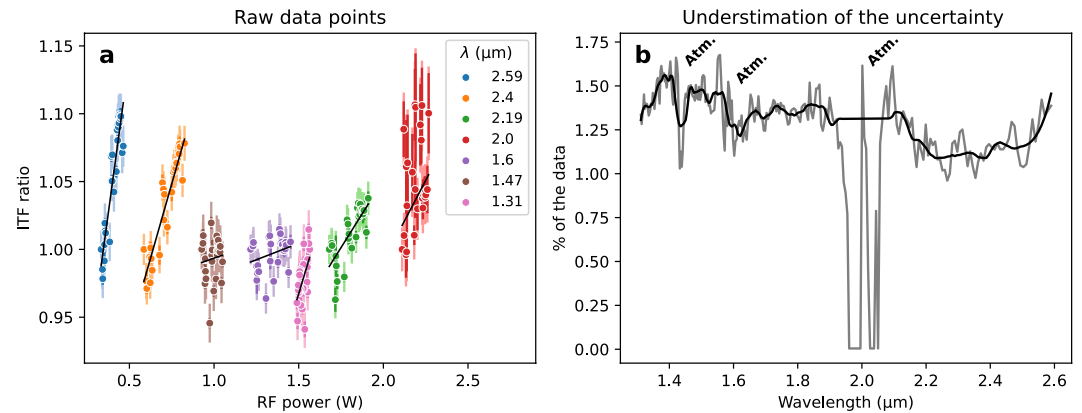
Then, data from a given observation  $X$  are converted into radiance using a similar relation:

$$I_X = \text{DN}_X / t_{\text{int}X} \text{ITF}_{20} \quad (5)$$

Finally, data are converted into relative reflectance by dividing by the radiance of an ideal white target in the same conditions using the same model as for the ITF definition:

$$\text{Ref}_X = \frac{I_X}{I_{\text{Sun},X}} \quad (6)$$

This reflectance calibration removes the main instrumental features, such as the spectral response of the detector, the AOTF efficiency, and the optics transmission, and it corrects the continuum position from the illumination geometry in terms of Mars-to-Sun distance and solar elevation. However, during the conversion into reflectance, we make no hypothesis on the target inclination with respect to the local vertical, since this parameter is mostly unknown. This introduces an incidence bias that affects estimation of the absolute reflectance. The only way to address this limitation would be to use a 3D geometric model of the target giving its real position in the workspace frame. Moreover, the atmospheric features are not removed from  $\text{DN}_{20}$  data because they are convolved by the instrument's response, and they cannot be simply eliminated by division. Thus, these features are only partially



**Figure 13.** (a) Instrumental transfer function (ITF) ratios as a function of radio frequency (RF) power (for clarity) and for several wavelengths across the spectral range. At a given wavelength (i.e., a given RF frequency set point), the RF power dispersion due to the IR board temperature variations is linearly correlated to the ITF ratio. The calculated uncertainty is represented by dark error bars and the underestimation assessment is the light bars. At 2.0 μm, the CO<sub>2</sub> residuals strongly increase the noise estimation. (b) Uncertainty underestimation as a function of wavelength. It decreases at wavelengths corresponding to atmospheric features because the noise there is greater.

corrected in science data by multiplication by the  $ITF_{20}$  and they require a further correction using a reference atmospheric spectrum on reflectance data to compensate for the difference of atmospheric properties (see Section 4.4.2).

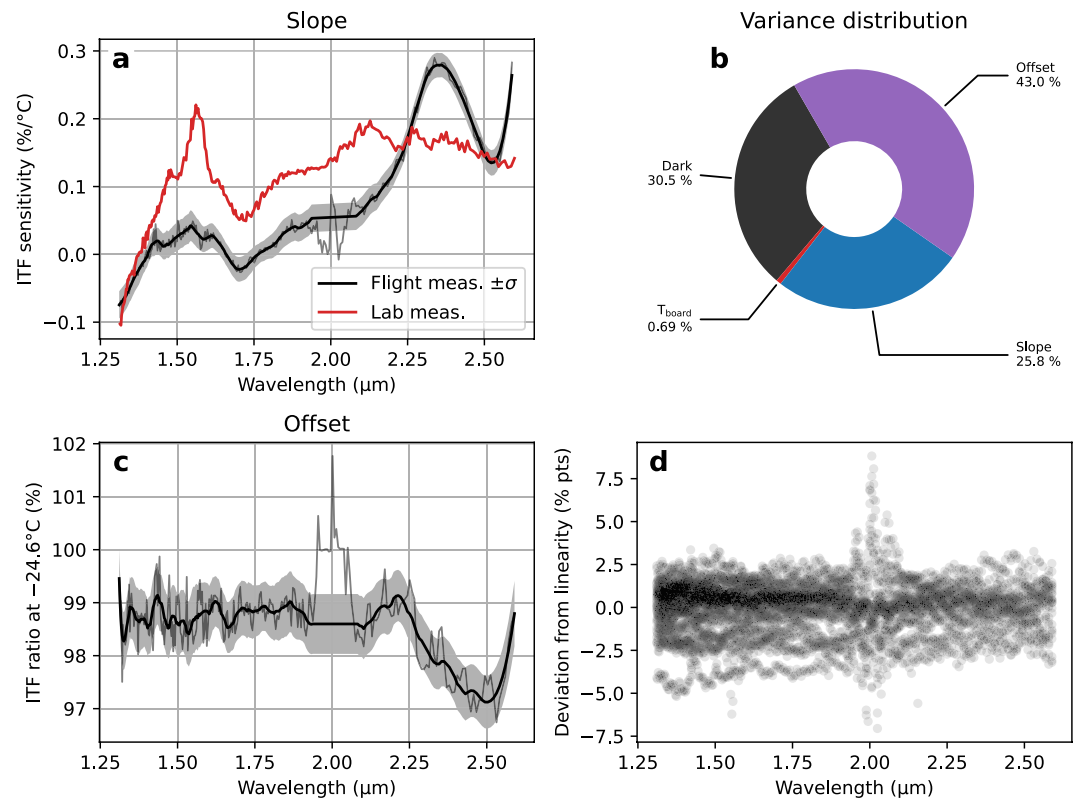
#### 4.2.2. Temperature Calibration

Regarding the dependence of the AOTF transmission on the injected RF power, the IRS FM on Mars is assumed to behave similarly as the FS (see Section 3.4), so we applied the linear power-to-transmission model to derive the calibration law. For this purpose, the curve fitting has been performed using a maximum-of-likelihood approach accompanied by a Bayesian and a Monte-Carlo by the Markov Chain algorithm to estimate the uncertainty on each fitting parameter. This method has already been used for the IRS FM ground calibration and is described in Royer et al. (2020). To calculate the instrument's transmission, instead of raw Signal-Dark differences, we favored the use of ITF ratios to take into account the variations of illumination conditions between the various IR White SCCT observations. The fit law is thus defined as follows:

$$\frac{ITF_{20}}{ITF_X} = A \times (T_{board_X} - T_{board_{20}}) + B \quad (7)$$

With  $A$  and  $B$  the slope and y-intercept of the linear law, called “Slope” and “Offset” hereafter. The Slope is thus the combination of the  $T_{board}$ -to-power and the power-to-transmission slopes, and the Offset should be constant and equal to 1 if no other instrumental bias is present. To assess the error on the Slope and the Offset, the algorithm uses the data uncertainty, taken as the combination of the noise and the precision of the  $T_{board}$  HK ( $\pm 0.5^\circ\text{C}$ ). The uncertainty on the illumination is evaluated afterward as an underestimation of the total uncertainty. The underestimation factor is thus taken as a fraction of the data and acts as a fitting parameter (Figure 13).

The result of the fitting algorithm and the final evaluation of the average error distribution are given in Figure 14. As expected, the IRS FM behaves differently from its FS, but both responses are of the same order of magnitude (Figure 14a). The Offset is not constant and equal to 1 but is shifted by 1.5%–2% and presents a  $T_{board}$  related 2.5 μm feature (Figure 14c). This residual is attributed to the dispersion of the ITF ratios due to the uncertainty on the illumination (Figure 14d). Finally, the distribution of the uncertainties on every measurement shows that the calibration is responsible for about 2/3 of the total error, the remaining being mostly attributed to the Dark; the uncertainty on  $T_{board}$  is negligible (Figure 14b). However, these two major sources are very different in terms of error statistics. Indeed, the Dark contribution is a stochastic noise, occurring at a high frequency (i.e., at the scale of a spectral channel), whereas the calibration contribution corresponds to low-frequency constant offset



**Figure 14.** Results of the infrared spectrometer Flight Model flight calibration. (a) Fitted Slope (gray line, black is smoothed), the red line is the lab measurement on the Flight Spare for comparison. (b) Average distribution of the error sources on every calibrated science observation (up to Sol 380). (c) Fitted Offset (gray line, black is smoothed). (d) Absolute deviation from model, in percent points, for every instrumental transfer function (ITF) ratio.

variations related to uncertainties on local illumination conditions and thermal shifts. This difference is of importance when we estimate the uncertainty on spectral parameters (Section 5).

Finally, the Slope and the Offset are smoothed to keep the low-frequency trend (higher frequency noise is already taken into account in the error bars) and the atmospheric features are ignored (Figures 14a and 14c, black lines). We thus derive a correction vector to the reflectance spectra by calculating  $ITF_{corr} = A \Delta T_{board} + B$  and apply it to science radiance data:

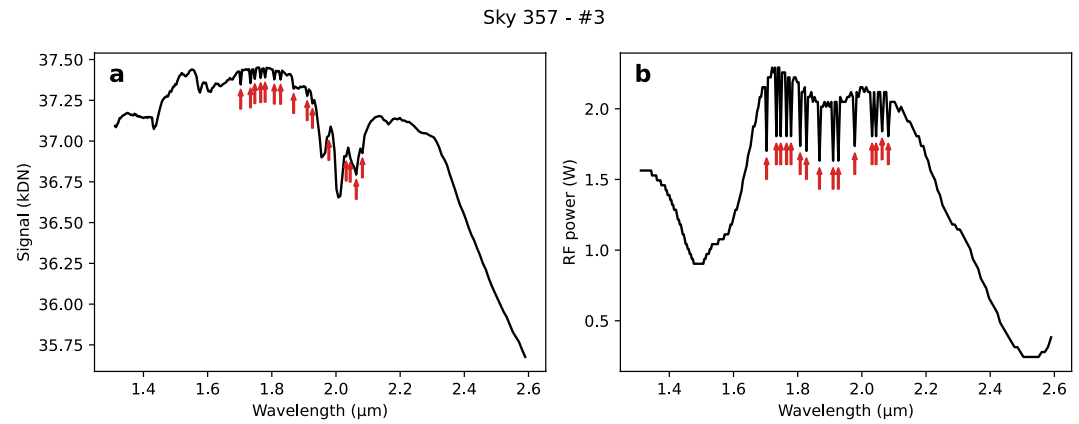
$$Ref_{corr} = \frac{Ref_x}{ITF_{corr}} \quad (8)$$

### 4.3. Glitches and Spikes

#### 4.3.1. Glitches

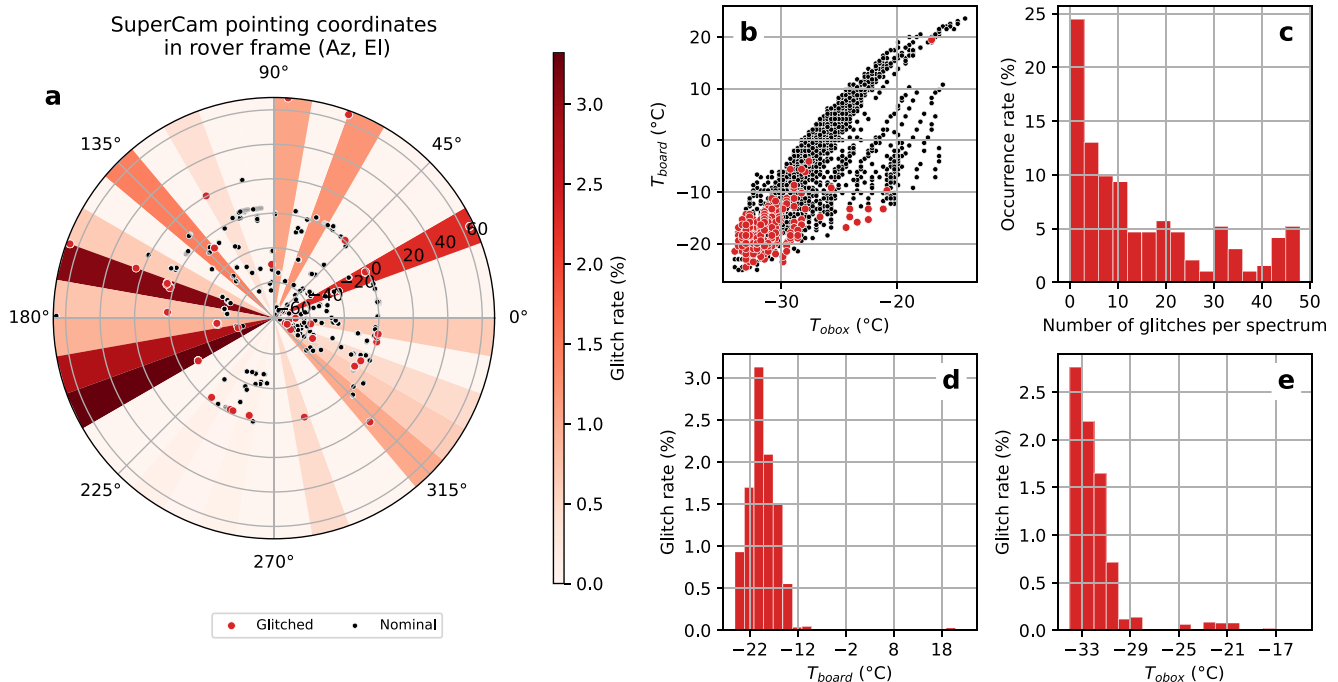
Glitches are artifacts occurring only when the AOTF is supplied by the RF signal, behaving as Signal drops of nearly constant amount, affecting only one spectral channel with very rare consecutive occurrences. They are also characterized by an easily detectable RF power counterpart (Figure 15). They are attributed to an EMI/EMC by the IRS itself or by another instrument onboard Perseverance.

Glitches were statistically studied to understand their behavior (Figure 16). It appeared that the glitches are not correlated with the Mast Unit elevation but they seem to be more frequent when the instrument points backward and in the 60° azimuth direction (rover frame, 0° corresponds to pointing straight forward, Figure 16a). The number of glitches per spectrum is mostly low, 25% of glitchy measurements have less than 3 glitches (Figure 16c), then it rapidly decreases toward high glitch rates. The most relevant parameter to describe the



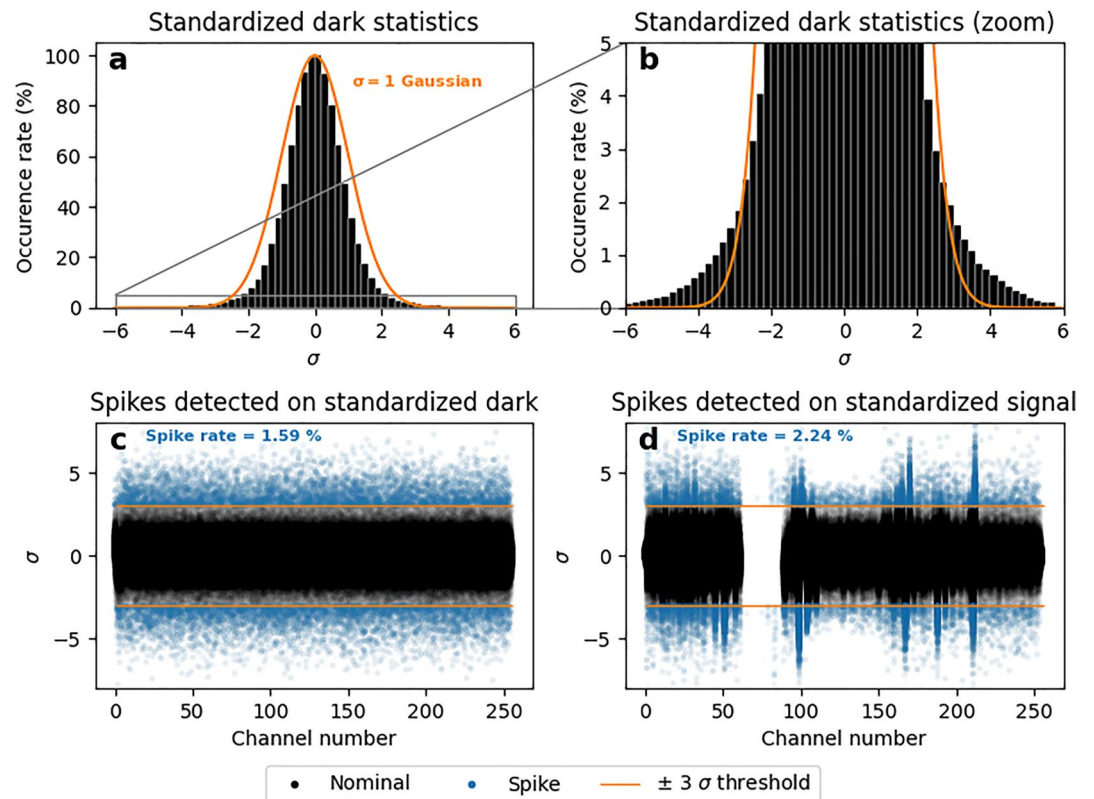
**Figure 15.** Example of glitchy passive Sky spectrum, acquired on Sol 357, 3rd point. (a) Raw Signal. Glitches are highlighted by a red arrow. The strong triplet at 2  $\mu\text{m}$  is the  $\text{CO}_2$  absorption lines convolved by the infrared spectrometer spectral response. (b) Radio frequency power counterpart of the glitches.

glitches is the temperature of the IR board (Figures 16b, 16d and 16e). Indeed, glitches are very well correlated with lower  $T_{\text{board}}$  with a maximum probability around  $T_{\text{board}} = -21^\circ\text{C}$  (3% chance for a spectral channel to be glitchy, a spectrum containing 256 channels in most cases). The correlation with the IR Optical box (OBOX) is due to the correlation between the temperatures of the IR board and the OBOX. Indeed, the IRS is cooler in the early morning than at midday and is heated by previous SuperCam activities. Thus, the operational use of SuperCam VISIR measurements leads to a trade-off between observing at the lowest temperature to have a lower Dark and noise and avoiding too cold temperatures to minimize the risk of having glitches.



**Figure 16.** (a) Spatial distribution of all SuperCam measurements in polar projection. Each point is a pointing direction, blacks are nominal measurements, and reds are glitchy. The red sectors correspond to the glitch rate (the number of glitches among the total number of acquired points, a spectrum containing 256 points in most cases) in a  $10^\circ$  azimuth window.  $0^\circ$  elevation corresponds to the horizon. (b) Distribution of all measurements in the  $(T_{\text{board}}, T_{\text{obox}})$  space. Red points are glitchy measurements. (c) Number of glitches per spectrum statistics on glitchy data. (d) Glitch rate distribution as a function of  $T_{\text{board}}$ , that is, the number of glitches among the total number of points in the  $2^\circ\text{C}$  interval. Panel (e) same as panel (d), but for  $T_{\text{obox}}$  and  $1^\circ\text{C}$  intervals.





**Figure 17.** (a) Standardized dark data distribution. The orange curve is a 1- $\sigma$  Gaussian centered on zero. (b) Zoom-in on the distribution feet to show the deviation from Gaussian. (c) Standardized Dark data with spikes detection using a 3- $\sigma$  threshold. Panel (d) same as panel (c), but for Signal. Atmospheric absorption bands have been masked because they bias the noise estimation.

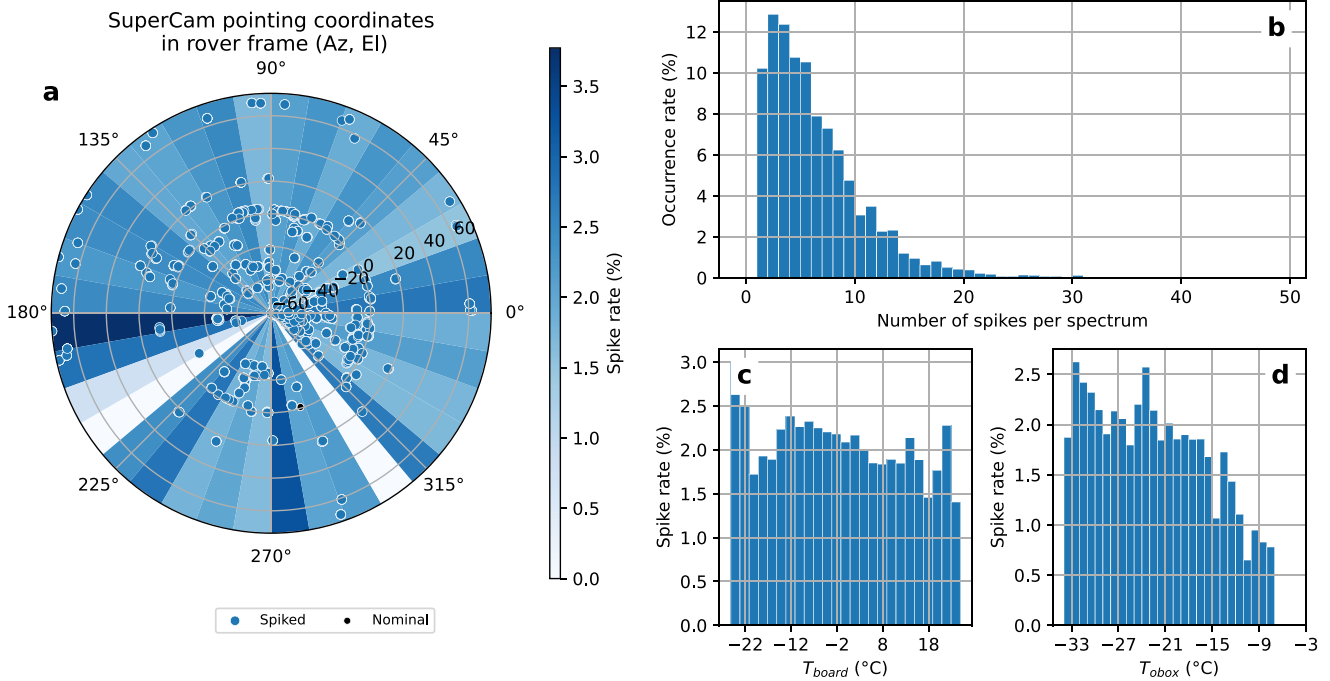
In the current (version 3) calibration pipeline, glitches are very efficiently detected on RF power curves so that they cannot be mistaken with real spectral features. Then, they are eliminated by linearly interpolating the neighboring nonglitchy points (glitches never occur on two adjacent channels). In the worst case, a spectrum could be glitchy on half of its spectral channels (every other channel) and the interpolation would then behave as a halving of the instrumental resolution. Thus, according to Shannon's sampling theorem, this will only affect the detection of the narrowest signatures (narrower than four times the spacing between the spectral channels).

#### 4.3.2. Spikes

Spikes are artifacts behaving as out-of-statistics noisy points. They are more easily detected on the Dark but they are also present on the Signal, independently of the Dark. They are identified by a 3- $\sigma$  filter on standardized data, corresponding to the probability to have at most one spike on a 256-channel spectrum, that is, an occurrence rate <0.4% (Figure 17). Their measured rate is about 4–5 times greater than the natural rate of 3- $\sigma$  events, showing their nonstatistical origin.

The study of their statistics shows that their occurrence is not correlated to the mast position (Figure 18a), neither to the thermal conditions (Figures 18c and 18d) nor to the glitches. However, the spikes seem less frequent at the high IR OBOX temperature. The distribution of their number is similar to a binomial distribution (Figure 18b), suggesting that their occurrence rate is constant along the acquisition of a spectrum, and thus, their origin is purely random.

After the spikes identification, their correction process is exactly the same as for the glitches.



**Figure 18.** (a) Spatial distribution of all SuperCam measurements in polar projection. Each point is a pointing direction, blacks are nominal measurements, and blues are affected by spikes. The blue sectors correspond to the spike rate (the number of spikes amongst the total number of points) in a 10° azimuth. A 0° elevation corresponds to the horizon. (b) Number of spikes per spectrum statistics. (c) Spike rate distribution as a function of  $T_{board}$ , that is, the number of spikes among the total number of points in the 2°C interval. Panel (d) same as panel (c), but for  $T_{obox}$  and 1°C intervals.

#### 4.4. Illumination and Atmosphere Models

##### 4.4.1. Illumination Model

As explained in the description of the calibration pipeline (Section 4.1), the ITF calculation as well as the conversion into reflectance rely on an illumination model. This model assumes that the only source of light is the direct solar illumination and it calculates the local solar flux reflected by an ideal white Lambertian target under the same conditions as the observation by

$$I_{\text{Sun}} = \frac{1}{\pi} \Omega_{\text{Sun}} \cos(i_{\text{Sun}}) \varepsilon_{\text{Sun}} u_{\lambda}(T_{\text{Sun}}) \quad (9)$$

where  $\Omega_{\text{Sun}} = \pi r_{\text{Sun}}^2 / d_{\text{Sun}}^2$  is the solid angle under which the Sun is seen from the target ( $r_{\text{Sun}}$  is the solar radius and  $d_{\text{Sun}}$  the Mars-to-Sun distance),  $i_{\text{Sun}}$  is the solar incidence on the target,  $\varepsilon_{\text{Sun}}$  is the solar emissivity, taken equal to 1, and  $u_{\lambda}(T_{\text{Sun}})$  is the solar spectral radiance given by the Planck's law. For the calculation of the astronomical parameters,  $d_{\text{Sun}}$  and  $i_{\text{Sun}}$ , we use an ephemeris model based on SPICE kernels. Martian ground targets are assumed as horizontal so the  $i_{\text{Sun}}$  is simply the solar zenith angle, directly given by the ephemeris. SCCTs are in a well-known geometry and the solar incidence onto them is calculated using the rover position quaternion and the Sun's coordinates in the site frame. Considering nonhorizontal targets would require knowing the direction of the surface normal, in azimuth and elevation. This information requires a 3D modeling of targets, which is not automatically performed. Moreover, at the scale of the IRS field of view, when the instrument observes rocks or pebbles, the surface is composed of many facets oriented in different directions and assuming that they are all oriented to the average rock/soil orientation would be as uncertain an approximation as assuming them to be horizontal.

Planck's law is an approximation of the real solar radiance but provides a physical meaning of the target radiance. Indeed, in the conversion into reflectance, this constant is removed by division. Thus, it does not affect the final result. Basically, the illumination model can be summarized as a partial photometric correction that includes solar distance and the incidence cosine ratio between the target and SCCT observation.

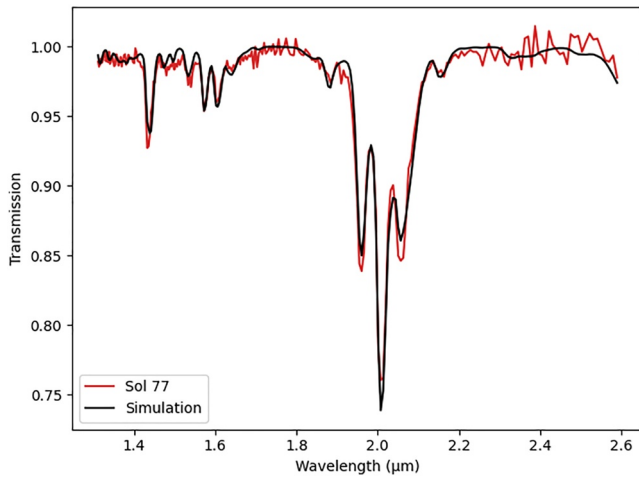


Figure 19. Atmospheric spectra used for the atmospheric correction.

However, an important geometric bias may remain owing to the assumption of a horizontal target. If the target is inclined by an angle  $\alpha$ , the real incidence  $i$  is given by  $\cos i = \cos(i_{\text{Sun}} - \alpha)$  and the resulting geometric error is  $\frac{\cos i}{\cos i_{\text{Sun}}} = \cos \alpha + \tan i_{\text{Sun}} \sin \alpha$ . The  $\alpha$  angle has to be calculated at the IRS field of view scale, which is about a few millimeters for the targets in the rover's workspace. Thus, it may strongly vary with the target's macroscale and microscale roughness, independently from its average inclination.

Another aspect of this model is that it considers the Sun as the unique source of light, and that no surrounding terrain reflects light on the target, and it neglects the potential diffusive contribution from the atmosphere. In the case of SCCT observations, the rover itself becomes a source of scattered light from its white paint and instruments in the SCCTs' field of view. Moreover, the rover white paint has several strong absorption features in the near IR that are observed in several SCCTs' spectra (Figure 23). A dedicated photometric model including this contribution would be required to address these artifacts.

#### 4.4.2. Atmospheric Absorption Correction

Through the  $\text{CO}_2$  absorption features, the atmosphere is one of the major contributors to the reflectance spectra. Its spectral features must be removed from ground target observations since they can influence mineral absorption bands. For example, the 1.9  $\mu\text{m}$  band (related to hydration) is strongly affected by the  $\text{CO}_2$  2  $\mu\text{m}$  triplet. This correction is performed on reflectance calibrated data in order to not be biased by the instrument response (Figure 11). The atmosphere is modeled as follows: before reaching SuperCam, the light is absorbed by the atmosphere from space to the target and from the target to the instrument. For any target, the first optical path is mostly the same as the one measured during the Sol 20 IR White SCCT reference observation but with some additional path lengths at lower sun angles. The second path is negligible for the workspace targets (which are only a few meters away), but it can be important for long-distance observations (hundreds of meters to kilometers). The atmospheric absorption is thus modeled as the division by a reference transmission spectrum raised to a given power to compensate the observation distance and the seasonal density variation:

$$\text{Ref}_{x, \text{atm}} = \frac{\text{Ref}_x}{t_{\text{atm}}^{k_{\text{atm}}}} \quad (10)$$

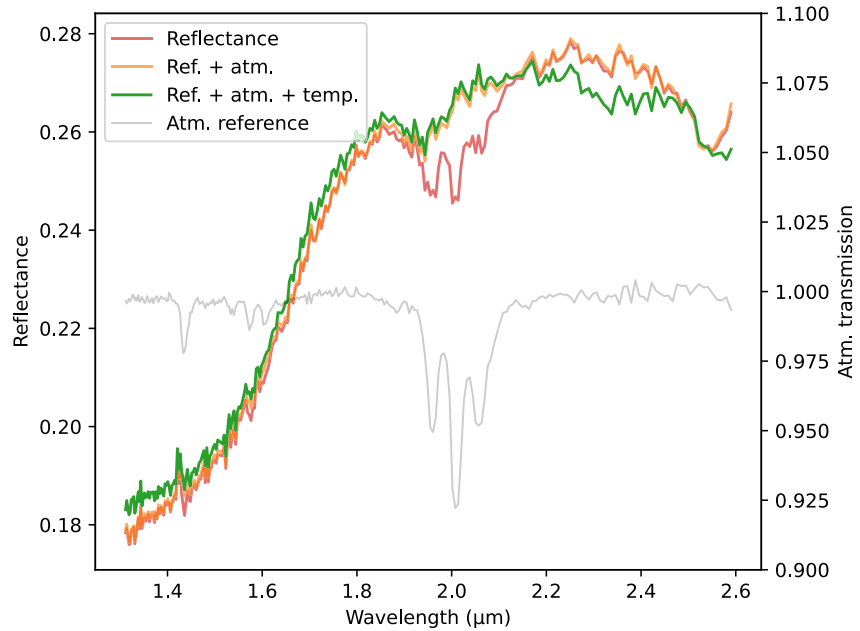
Two reference transmission spectra,  $t_{\text{atm}}$ , are used in the current pipeline: a modeled  $\text{CO}_2$  spectrum convolved by the IRS spectral response and an atmospheric spectrum derived from the Sol 77 passive sky observation (Figure 19).

The  $k_{\text{atm}}$  parameter is calculated by minimizing the variance of the  $\text{Ref}_{x, \text{atm}}$  vector in the atmospheric feature ranges (mainly between 1.9 and 2.1  $\mu\text{m}$ ). The minimal variance corresponds to the best elimination of the features, and the reference spectrum leading to the lowest variance is kept for the calibration (Figure 20).

#### 4.5. Calibration Validation

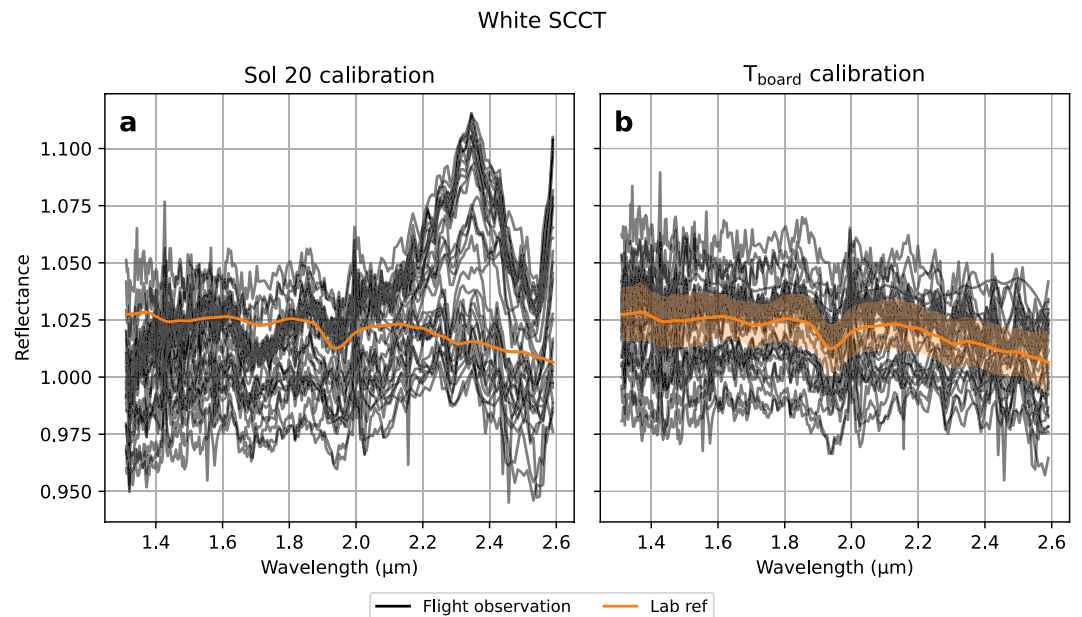
A first validation of the  $T_{\text{board}}$  calibration is performed by recomputing the reflectance of every IR White SCCT observation, previously shown in Figure 7. The result is very satisfying since  $T_{\text{board}}$ -related spectral features are not visible anymore and the data dispersion is identical to Figure 14d (Figure 21).

A proper validation comes with the calibration of Color SCCTs, acquired several times during the mission (Figure 22). These targets are mostly Lambertian; thus, they are suitable for a recurring observation under various illumination conditions. Three Color targets are used for this validation: Cyan, Red, and Black, each of which includes an embedded magnet, to decrease the magnetic dust contamination (Cousin et al., 2022; Manrique et al., 2020). We used observations of the Cyan SCCT from Sols 77 and 246, two observations of the Black target from Sol 11 and one from Sol 77, and one from Sol 77 for the Red target. The Cyan and Red SCCTs absolute levels were in good agreement with their lab reference and the two Cyan observations overlapped each other,

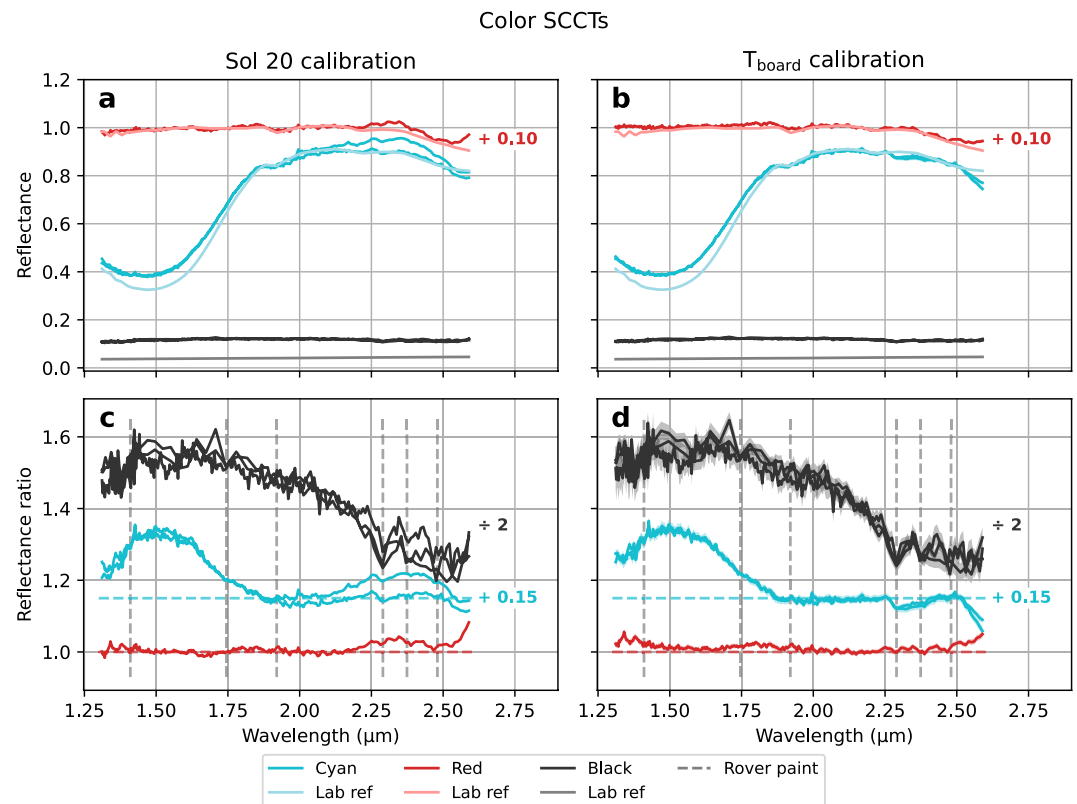


**Figure 20.** Reflectance of a long distance target observed on Sol 147 (sequence scam06147, 9th point) at different calibration stages: raw reflectance conversion (red), after atmospheric correction (orange), and after thermal correction (green). In the calibration pipeline, the thermal correction step is performed on radiance, not on reflectance, but it is shown here to highlight its effect. The used atmospheric spectrum at the optimal exponent is given in light gray.

showing the accuracy of the illumination model (Figures 22a and 22c). However, the Black SCCT and the broad 1.5 μm absorption feature of the Cyan were more poorly reproduced by the IRS (although the latter exhibits few spectral features and has very low reflectance). The thermal calibration increases the agreement with the lab spectra and the overlapping of various measurements of the same target, except for the Red at a short wavelength



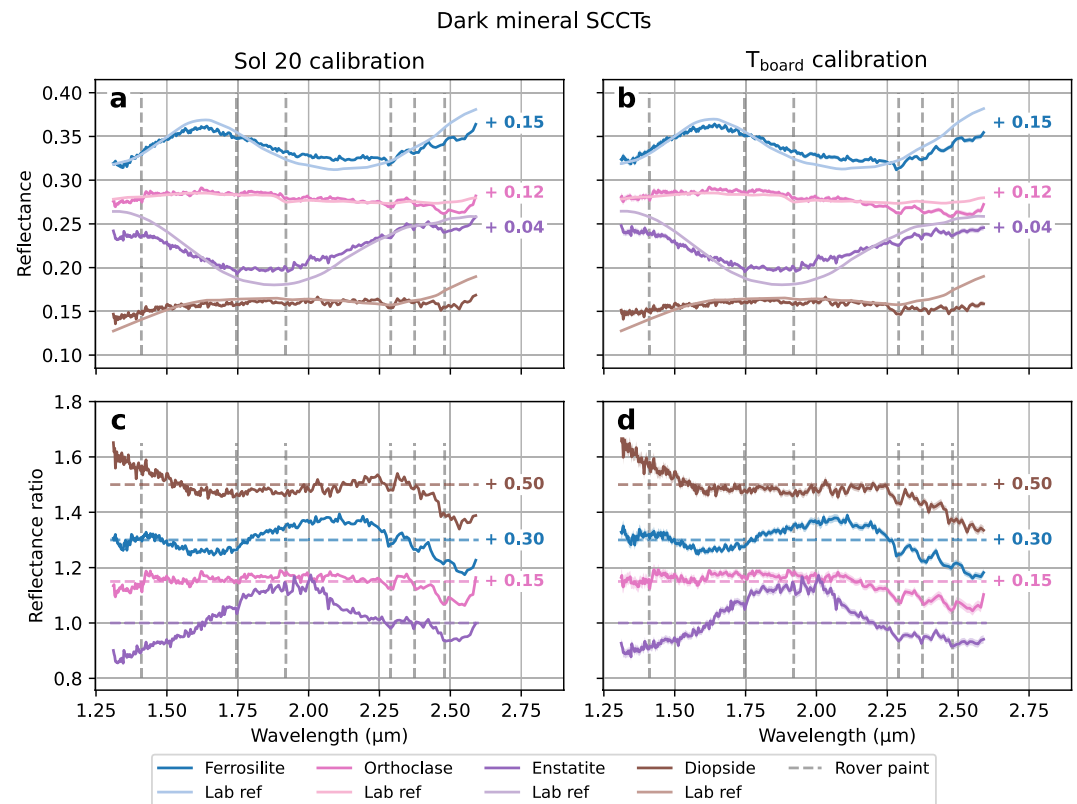
**Figure 21.** Calibration of all infrared White SuperCam Calibration Target (SCCT) observations. (a) Using the zero-order calibration only. Orange line is the lab reflectance of the target. (b) Thermal calibration, the orange transparent area represents the maximum error on the whole set of white calibrated spectra. The remaining vertical dispersion is greater than the calibration error; thus, it is attributed to the uncertainty on local illumination geometry and AluWhite's non-Lambertian nature, and not the calibration itself.



**Figure 22.** Color SuperCam Calibration Targets (SCCTs) calibration: Red on Sol 77, Cyan on Sols 77 and 246, and Black on Sols 11 (2 times) and 77. (a) Reflectance spectra calibrated with the Sol 20 ITF only. The corresponding lab reference is given in lighter color. The red spectra are vertically shifted for clarity. Panel (b) same as panel (a), but after the thermal calibration. (c) Measurement to lab reference ratios. The black curves are divided by 2 (reference baseline is thus off-axis) and Cyan ones are shifted for clarity. Dashed vertical lines correspond to the positions of the rover white paint absorption features. Panel (d) same as panel (c), but after the thermal correction. The significant difference between the flight measured and lab spectra of the Black SCCT, and in the absorption feature of the Cyan SCCT, could be attributable to an instrument nonlinearity with the incoming flux. A dedicated measurement campaign would be required to characterize this effect but has not been performed yet.

(1.3–1.4  $\mu\text{m}$ ) and the Cyan at a long wavelength (2.55–2.6  $\mu\text{m}$ ) (Figures 22b and 22d). Rover white paint absorption features are visible on Black and Cyan spectra, which show that the contribution of the light reflected by the rover is not negligible and could be an additional light source to be taken into account for the reflectance calculation. However, this reflected compound has never been observed in Martian observations and no correlation has been found between the 2.28  $\mu\text{m}$  band (strongest rover paint feature) observed in the rocks of the *Mááz* formation (see Section 5.2) and the target-rover distance or the illumination conditions.

A series of mineral SCCTs (i.e., not color SCCTs: Ferrosilite, Orthoclase, Enstatite and Diopside, see Cousin et al., 2022; Manrique et al., 2020) was acquired on Sol 79 to characterize their flight spectral response and validate again the IRS response on known rock samples. The main difference with color targets is that the mineral ones are not Lambertian and the absolute reflectance cannot be compared directly to their lab values. Nonetheless, the main spectral features of each mineral are well reproduced (Figure 23) and the thermal calibration efficiently removes the 2.5  $\mu\text{m}$  aberrant feature (well visible in Figure 21a for example). Similarly to the color SCCT, some rover white paint absorption bands are visible in mineral SCCTs' spectra (particularly upon ratioing to their lab spectra), which indicate a contamination under these specific illumination conditions. The main absorption feature of the rover paint is the 2.28  $\mu\text{m}$  band (Figure 2), which can be mistaken with the Fe–OH absorption of phyllosilicates. But we found no correlation between the measured 2.28  $\mu\text{m}$  band depth in the Crater Floor and the distance to the rover or the illumination geometry (which could illuminate a white painted rover surface scattering onto the target).



**Figure 23.** Mineral SuperCam Calibration Targets (SCCTs) calibration. Data acquired on Sol 79. (a) Reflectance spectra calibrated with the Sol 20 ITF only. The corresponding laboratory reference is given in lighter color. Due to the non-Lambertian nature of these targets, their lab reflectance reference has been rescaled to the average flight measurement and both are shifted for clarity (the corresponding value is indicated on each panel). Panel (b) same as panel (a), but after the thermal calibration. (c) Measurement to lab reference ratios. Dashed vertical lines correspond to the positions of the rover white paint absorption features (Figure 2). Panel (d) same as panel (c), but after the thermal correction.

As a conclusion, the IRS radiometric calibration and its thermal correction allow a high fidelity retrieval of mineral spectral signatures as well as an estimation of the absolute reflectance in a good agreement with the expected lab measurements. However, calibration residuals are still present, although acceptable for mineralogical identification, and the rover white paint may be an additional minor source of light biasing the estimation of the illumination conditions and therefore the ITF derivation. Further investigations on a more realistic illumination model are necessary to address this point.

## 5. IRS Spectral Performance

### 5.1. The Band Depth-To-Noise Ratio Estimate

The SNR is the main quantity that allows us to evaluate the quality of the data and the validity of the absorption band detections. Thanks to the results of the radiometric calibration, we can precisely define the SNR of a reflectance spectrum but also the band depth-to-noise ratio (BDNR) associated with an absorption band or a spectral parameter.

In general, for a given spectral channel, the SNR is defined as the ratio between the reflectance of this spectral channel and the local uncertainty derived from the calibration. As detailed in Section 4.2, this uncertainty contains different contributions affecting the data at different scales. The Dark-related noise is an uncorrelated noise, varying randomly across the spectral channels (the one studied in Section 3.2), while the uncertainty determined by modeling the temperature sensitivity of the instrumental transmission is highly correlated. This last point means that if we compare the reflectance of two close spectral channels (labeled  $Sp_1$  and  $Sp_2$ , directly

contiguous or separated by less than a dozen channels), in a band depth calculation for instance, only the variance of the Dark must be taken into account. In other words:

$$\text{Var}(Sp_1 - Sp_2) = \text{Var}(Sp_1) + \text{Var}(Sp_2) - 2 \text{Cov}(Sp_1, Sp_2) \quad (11)$$

$$= \text{Var}(Sp_1)_{\text{Dark}} + \text{Var}(Sp_1)_{\text{model}} \quad (12)$$

$$+ \text{Var}(Sp_2)_{\text{Dark}} + \text{Var}(Sp_2)_{\text{model}}$$

$$- 2 \text{Cov}(Sp_1, Sp_2)_{\text{model}}$$

Because uncertainties related to the Dark and the model are independent and  $\text{Cov}(Sp_1, Sp_2)_{\text{Dark}} = 0$ . Moreover, by the correlation of the model's uncertainty, we have  $\text{Cov}(Sp_1, Sp_2)_{\text{model}} \sim \text{Var}(Sp_1)_{\text{model}} \sim \text{Var}(Sp_2)_{\text{model}}$ . Thus,

$$\text{Var}(Sp_1 - Sp_2) = \text{Var}(Sp_1)_{\text{Dark}} + \text{Var}(Sp_2)_{\text{Dark}} \quad (13)$$

In summary, the SNR is defined in accordance with the accuracy objective of the instrument given during its design and ground calibration (Royer et al., 2020). When evaluating absolute accuracy, the SNR is defined as a ratio of the signal and the uncertainty taking into account the Dark and the calibration. This uncertainty is given in the “QUALITY” extension of the files delivered to NASA Planetary Data System. When evaluating the relative precision, that is, for contiguous spectral channels, the SNR is defined using the noise of the Dark only (see Equation 13), itself evaluated by calculating the variance of Dark measurements. This second definition is also applied when calculating the depth of narrow bands, that is, sampled with less than about 10 spectral channels.

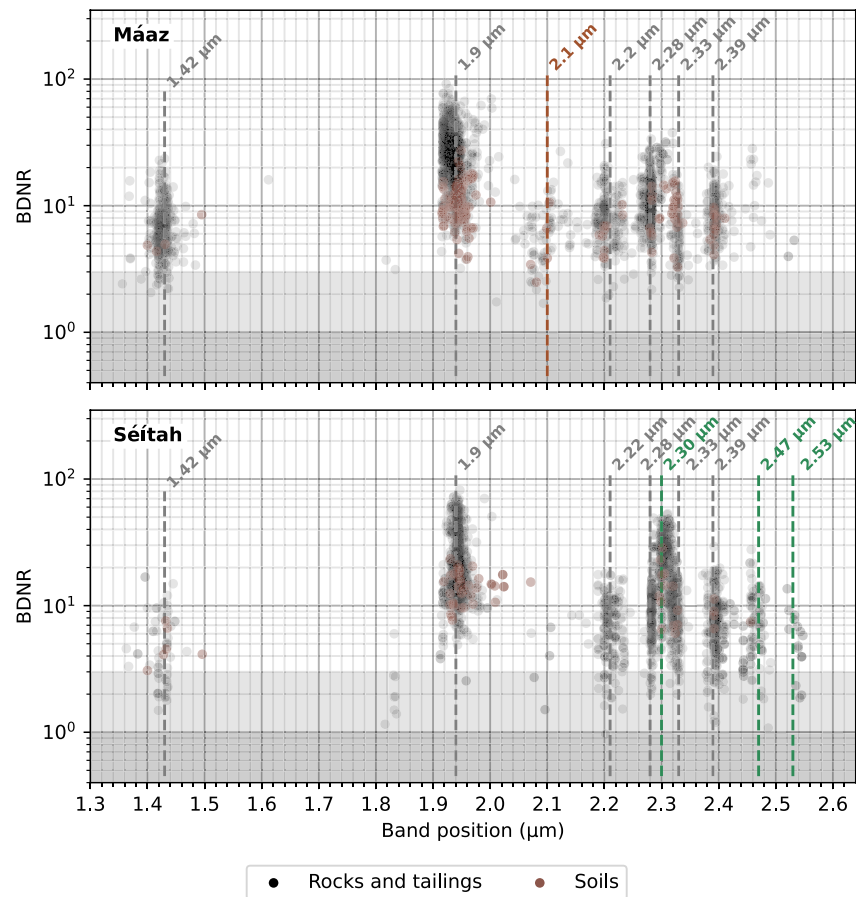
## 5.2. Observed Absorption Features

From landing to the end of the Crater Floor Campaign (Sol 379), two geological units were explored by the rover. Perseverance landed on the *Máaz* formation. This is the largest unit on the crater floor, it has a rough, rock-covered surface, and exhibits a crater-retaining morphology compared to the adjacent *Séítah* formation. This second geological unit is covered by numerous sand dunes and is stratigraphically lower than the *Máaz* unit. These two units are more extensively described in Farley et al. (2022) and Wiens et al. (2022).

Approximately 2,600 spectra have been acquired by the IRS on a wide variety of targets through Sol 379: dark-toned rocks, pitted rocks, holey rocks, pavers, coarse and fine soils, drill cuttings, abraded surfaces, and outcrops at long distances (for which various materials can be mixed within the field of view). The method for calculating the position and depth of each absorption band is described in Mandon et al. (2022). We summarize here the main results in order to evaluate their accuracy from the calibration results. Indeed, the statistical analysis of the ITF behavior (Section 4.2) allowed us to estimate the accuracy of the data reduction procedure and thus to deduce the error bars affecting each measurement, according to the conditions in which they were performed. In general, low albedo targets will be dominated by Dark instrumental noise, while bright targets will be more limited by the accuracy of the calibration itself.

The set of absorption band detections is summarized in Figure 24. These signatures are attributed to various silicates, phyllosilicates, salts, and iron-oxides/hydroxides. These phases are crucial markers of the aqueous processes that shaped the *Séítah* and *Máaz* formations. We list below the absorption bands detected in each unit, in the near-IR, along with their mineralogical assignment and an assessment of the precision of the detections. Mandon et al. (2022) provide a complete study of these spectral features and propose various mineral assemblages to explain them. Both units are characterized by the presence of a variety of spectral signatures related to aqueous alteration (1.4, 1.9, and 2.1–2.5  $\mu\text{m}$  bands) but they differ by nature of their alteration minerals: *Máaz* is dominated by the signatures of Fe-oxyhydroxides and Fe-bearing phyllosilicates (2.28  $\mu\text{m}$  Fe–OH band, Table 2), whereas *Séítah* additionally contains spectral features related to Mg-bearing phyllosilicates and presumably carbonates (2.3 and 2.5  $\mu\text{m}$  bands, Table 234).

The BDNr of the detections, defined as the ratio of the band depth and the local variance (see Section 5.1), varies strongly depending on the absorption band considered. In general, a high BDNr corresponds to a deep absorption band and/or a low noise measurement (intense illumination, bright target). The band at 1.9  $\mu\text{m}$  (related to the presence of molecular water) is almost omnipresent in the targets of *Séítah* and *Máaz* with a very high BDNr, except in the holey rocks where it is practically absent probably because of photometric effects, see Mandon



**Figure 24.** Position and signal-to-noise ratio (SNR) of every detected and visually confirmed absorption feature in the near-infrared in each geological unit. The colors indicate the general nature of the targets: brown = soils, black = workspace rocks and their drilling cuttings. Grayed areas correspond to SNR < 3 (light gray), meaning a greater detection uncertainty; and SNR < 1 (gray), no detection. The position of the main absorption bands is indicated with a color difference to highlight the bands specific to each unit (in green for *Séítah* and in brown for *Máaz*).

et al. (2022). On the other hand, the bands diagnostic of specific secondary phases between 2.1 and 2.5  $\mu\text{m}$  are weaker: they are shallower than the 1.9  $\mu\text{m}$  band, which explains the BDNR difference. Many measurements have a low BDNR, close to 2 or 3, which indicates uncertain detections that are difficult to distinguish among noise, instrumental artifacts, or real mineralogical signatures. Indeed, in this range of wavelengths, the spectral sampling is compared to the width of the absorption bands sought. Their detection corresponds to a signal drop on one or two spectral channels. However, most of the detections have a higher BDNR and are unambiguously identified (see Mandon et al., 2022).

### 5.3. Spectral Parameters Performance

When studying infrared spectra, spectral parameters are often used to evaluate the presence of absorption features and quantify their characteristics. Viviano et al. (2014) defined a multitude of spectral parameters adapted to the spectra provided by the CRISM instrument (*Compact Reconnaissance Infrared Spectrometer for Mars*) on board the *Mars Reconnaissance Orbiter* probe. We present here a method of adaptation of some of these parameters to the characteristics of the IRS and an evaluation of their performance, thanks to the error bars provided by the radiometric calibration of the instrument. The parameters used are, generically, the measurement of the depth of a narrow absorption band, the characterization of the shape of a broad band, and the measurement of a spectral slope.



**Table 2**  
*List of Near-Infrared Absorption Bands Detected in the Two Geological Formations Explored by the Rover*

Band center ( $\mu\text{m}$ )	Attribution	BDNR
<i>Máz</i>		
1.42	OH, H <sub>2</sub> O	2–20
1.9 (variable)	H <sub>2</sub> O	>10, up to 100
2.13 (“flat”)	Mg monohydrated sulfate/perchlorate	3–10
2.2	Al–OH/hydrated silica/gypsum	3–10
2.28	Fe–OH	4–30
2.32–2.33	Mg–OH (phyllosilicate)	3–15
2.39	Fe/Mg–OH	3–20
<i>Séítah</i>		
1 (wide)	Olivine, pyroxene, and Fe-bearing phases	>1,000
1.42	OH, H <sub>2</sub> O	2–10
1.9 (variable)	H <sub>2</sub> O	>10, up to 100
2.2	Al–OH/hydrated silica	1.5–5
2.28	Fe–OH	2–15
2.30	Fe/Mg–phyllosilicate and/or carbonates	4–50
2.32–2.33	Fe/Mg–phyllosilicate and/or carbonates	2–20
2.39	Fe/Mg–OH	1.5–20
2.47	Possibly talc	2–15
2.53	Carbonates	Mostly <3 but some 3–8 were confirmed

*Note.* The BDNR column corresponds to the evaluation of the detectability of the bands from the observations made and the performance of the instrument. These values indicate the confidence level in each detection: BDNR <1 = no detection, 1 < BDNR <3 = faint detection. The band at 1  $\mu\text{m}$  is outside the IRS spectral range but is broad enough to be measured via its right wing. The attribution column corresponds to the mineral phase or chemical bond associated with each feature detected in the context of the Crater Floor.

### 5.3.1. Narrow Band Depth

This kind of spectral parameter is defined by the reflectance at three wavelengths: the central wavelength ( $\lambda_C$ ) and “short” and “long” wavelengths taken at the band’s shoulders, where the continuum is evaluated ( $\lambda_S$  and  $\lambda_L$ ). Then, the band depth is simply derived by calculating (Viviano et al., 2014, Equations 2 and 3):

$$\text{BD}_C = 1 - \frac{R_C}{R_{C^*}} \quad (14)$$

where  $R_x$  is the reflectance at a given wavelength ( $C$ ,  $S$ , or  $L$ ),  $R_{C^*} = a R_S + b R_L$  is the value of the continuum projected at the central wavelength,  $a = 1 - b$  and  $b = \frac{\lambda_C - \lambda_S}{\lambda_L - \lambda_S}$  are weighting coefficients representing the fact that the absorption band is not necessarily symmetrical. In the case of the IRS, this definition can be taken as it is, only by substituting  $C$ ,  $S$ , and  $L$  by their corresponding values. The determination of the precision, at first order, of such a parameter is also straightforward. Indeed, for narrow bands, like in the 2.1–2.5  $\mu\text{m}$  region, we can approximate the reflectance of the continuum at the band’s shoulders to its average value  $R_{C^*}$ . Therefore, the precision of the spectral parameter is given by a quadratic weighted average of the local SNR and the band depth through:

$$\begin{aligned} \sigma_{\text{BD}}^2 &= \frac{\sigma_{R_C}^2}{R_{C^*}^2} + \frac{R_C^2}{R_{C^*}^4} \left( a^2 \sigma_{R_S}^2 + b^2 \sigma_{R_L}^2 \right) \\ &= (1 - \text{BD})^2 \text{SNR}_C^{-2} + (1 - \text{BD})^2 \frac{1}{R_{C^*}^2} \left( a^2 \sigma_{R_S}^2 + b^2 \sigma_{R_L}^2 \right) \\ &\sim (1 - \text{BD})^2 \left( \text{SNR}_C^{-2} + a^2 \text{SNR}_S^{-2} + b^2 \text{SNR}_L^{-2} \right) \end{aligned}$$

Thus,

$$\sigma_{BD} = (1 - BD) (\text{SNR}_C^{-2} + a^2 \text{SNR}_S^{-2} + b^2 \text{SNR}_L^{-2})^{0.5} \quad (15)$$

For example, the BD2355 parameter (Viviano et al., 2014, Tables 2–39), measuring the depth of the 2.355  $\mu\text{m}$  band, can be defined by

$$\text{BD2355} = 1 - \frac{R_{SP26}}{0.626 R_{SP33} + 0.374 R_{SP15}} \quad (16)$$

where  $R_{SPXX}$  is the reflectance of the XXth spectral channel. The precision of this parameter is given by

$$\sigma_{\text{BD2355}} = (1 - \text{BD2355}) (\text{SNR}_{SP26}^{-2} + 0.391 \text{SNR}_{SP33}^{-2} + 0.140 \text{SNR}_{SP15}^{-2})^{0.5} \quad (17)$$

All the values necessary to calculate these precision levels are given in the data products of every observation released in the NASA Planetary Data System by the SuperCam project.

### 5.3.2. Broadband Parameters

Broadbands show a variety of shapes that can be affected by a variation of the continuum itself. For this reason, their spectral parameters are defined as a linear combination of band depth measurements at various wavelengths with the same continuum definition (Viviano et al., 2014, Equation 7):

$$\text{BD}_{C_0-C_N} = \sum_{i=1}^N D_i \text{BD}_{C_i} \quad (18)$$

where the  $D_i$  are weighting coefficients such that  $\sum D_i = 1$ .

In this case, each band depth calculation being independent from the others, the precision at the first order of the spectral parameter is easily calculated ( $\lambda_S$  and  $\lambda_L$  being the same for every reference points):

$$\sigma_{\text{BD}_{C_0-C_N}}^2 = \sum_{i=1}^N D_i^2 \sigma_{\text{BD}_{C_i}}^2 \quad (19)$$

$$= \sum_{i=1}^N D_i^2 (1 - \text{BD}_{C_i})^2 (\text{SNR}_{C_i}^{-2} + a^2 \text{SNR}_S^{-2} + b^2 \text{SNR}_L^{-2}) \quad (20)$$

### 5.3.3. Slope Parameters

In addition to the characterization of the shape and depth of the absorption bands, the slope of the spectral continuum contains information about the nature of the rock. A slope parameter can be basically defined through two reflectance values, at “short” and “long” wavelengths, by

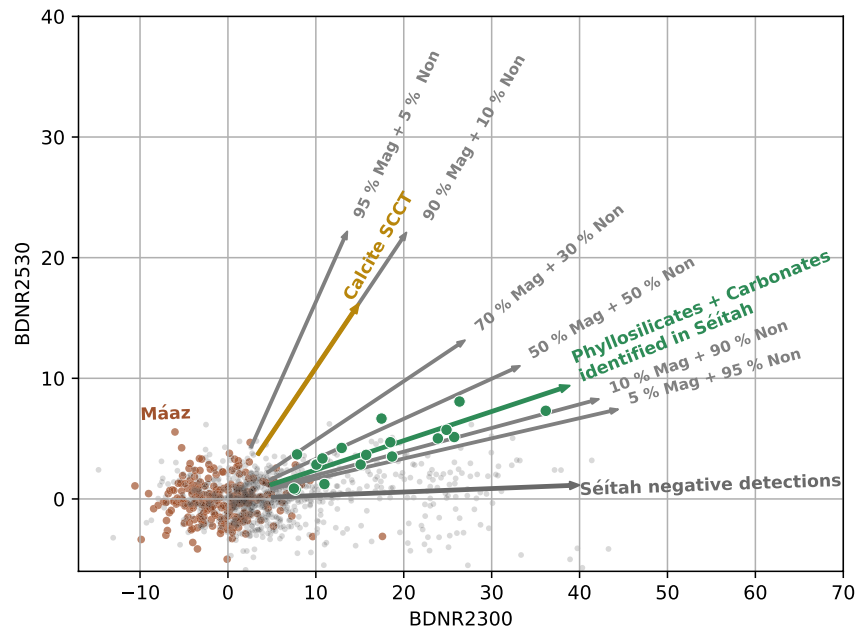
$$S_{S-L} = \frac{R_L - R_S}{\lambda_L - \lambda_S} \quad (21)$$

And, its precision is given by

$$\sigma_{S_{S-L}} = \frac{(\sigma_{R_L}^2 + \sigma_{R_S}^2)^{0.5}}{\lambda_L - \lambda_S} \quad (22)$$

### 5.3.4. Reflectance Smoothing

In order to increase the precision of the spectral parameters, a common procedure is to smooth the reflectance by taking the mean or median of a given set of spectral channels (typically 3 to 5). Thanks to the acquisition mode of an AOTF where the spectral channels are successively measured, each wavelength is independent from its neighbors. Therefore, when calculating a spectral parameter, if the smoothing kernel has a size  $N$ , then  $\overline{\sigma_{BD}} = \sigma_{BD} / \sqrt{N}$ .



**Figure 25.** Correlation between the band depth-to-noise ratio (BDNR) of the 2.30 and 2.53  $\mu\text{m}$  features for all the observations of the Crater Floor Campaign (black dots). Green points correspond to the phyllosilicate/carbonate mixtures confirmed by laser induced breakdown spectroscopy (Clave et al., 2022) and brown points are the targets from the Máaz unit. Arrows represent the 2.53/2.30  $\mu\text{m}$  trend (in green for carbonate-rich points in Séítah, in yellow for the Calcite SuperCam Calibration Target (SCCT) observations and in dark gray for the Séítah's negative detections) and are compared to lab reference magnesite/nontronite mixtures (in gray, Mag = magnesite, Non = nontronite). The six laboratory references are *c1be232*, *c1be233*, *c1be234*, *c1be235*, *c1be236*, and *c1be237* from the Planetary Data System Geosciences database.

#### 5.4. Example of Application: The Study of Clay/Carbonate Mixtures

The presence of carbonates in the IRS spectra is mainly highlighted by the two absorption bands of the  $\text{CO}_3$  group: at 2.3 and 2.5  $\mu\text{m}$ . However, some phyllosilicates (Fe/Mg-smectite clays, in particular) also show an absorption band around 2.3  $\mu\text{m}$ , which leads to difficulties in the determination of the nature of the observed phases.

The results of the radiometric calibration of IRS allow to study more precisely the end of its spectral range and the correlation between the depth of the bands at 2.3 and 2.5  $\mu\text{m}$ . We thus defined a specific BD2530 parameter targeting the 2.53  $\mu\text{m}$  band of Ca-carbonates and Fe/Mg-carbonates mixtures such that  $R_C = R_{\text{SP6}}(2.53 \mu\text{m})$ ,  $R_S = R_{\text{SP3}}(2.56 \mu\text{m})$ ,  $R_L = R_{\text{SP9}}(2.50 \mu\text{m})$ . This definition of the spectral parameter was developed to detect the weak absorption bands present at 2.53  $\mu\text{m}$ , taking into account the performance of the IRS in terms of noise and spectral sampling. In addition to the band depth study, we computed the BDNR of the parameter, which is more relevant to detect faint features in a noisy environment.

In the Crater Floor Campaign, the selection of observations with the highest BDNR of the 2.5  $\mu\text{m}$  band ( $>4$ ) forms a clear trend toward carbonate/phyllosilicate mixtures with low carbonate content. This feature is only observed in Séítah where the points responding positively to the spectral criterion form a trend above the unit average. The rest of the measurements in this unit form a continuum of trends from negative and zero slopes (absence of a band at 2.53  $\mu\text{m}$ , and noise effect) to the highest slopes, which would correspond to a progressive enrichment of phyllosilicate/carbonate mixtures. In contrast, the Máaz unit does not present any trend nor correlation (Figure 25). The band depth ratio does not depend only on the composition of the mixture but also on the grain size ratio between the two compounds. Thus, we cannot deduce the exact abundance of carbonate by comparing the trends. We can reasonably assume that it is low (i.e., there are more phyllosilicates than carbonates). This result is consistent with *Perseverance's* PIXL and SHERLOC analyses and modal mineralogy unmixing. More precisely, SHERLOC investigation mostly found Fe/Mg-carbonates in relation to olivine detection (Scheller et al., 2022a, 2022b), which is consistent with the IR band position at 2.53  $\mu\text{m}$ , attributed to Fe-carbonate. PIXL also found that these carbonate phases probably replace olivine grains, suggesting an alteration by dissolution of ultramafic minerals

and not a cementation around grains (Liu et al., 2022; Tice et al., 2022). Moreover, its quantification indicates an areal carbonate abundance of less than 20%, which is consistent with IR modal mineralogy (Poulet et al., 2022). These carbonate detections by IRS are also consistent with LIBS and Raman results (Clave et al., 2022).

## 6. Conclusion

The calibration of a space instrument is an essential step during its development but also during its scientific operations. In particular, radiometric calibration allows reducing the raw data into high-level scientific products with the minimum of instrumental biases and artifacts. In the case of the IRS on SuperCam, calibration required fine modeling of the instrument to understand its flight behavior, which is different from the results of pre-launch studies. This study allowed us to develop a complete automatic data reduction pipeline, the products of which are provided to the NASA Planetary Data System.

The main success of this flight calibration is the characterization and correction of the temperature dependence of the instrumental response of its power electronics. This last step allowed the study of the absorption bands at the end of the spectral range (2.5–2.6  $\mu\text{m}$ ) and the identification of the diagnostic signatures of carbonates. By correlating these signatures, which are also present in some phyllosilicates, we have shown that the carbonate-bearing alteration phases observed in the Crater Floor would be clay-carbonate mixtures with a minor carbonate content.

## Appendix A: The SuperCam Team

R. C. Wiens<sup>1</sup>, S. Maurice<sup>2</sup>, T. Acosta-Maeda<sup>3</sup>, C. Alvarez-Llamas<sup>4</sup>, R. B. Anderson<sup>5</sup>, S. M. Angel<sup>6</sup>, D. M. Applin<sup>7</sup>, G. Arana<sup>8</sup>, M. Bassas-Portus<sup>9</sup>, R. Beal<sup>10</sup>, P. Beck<sup>11</sup>, K. Benzerara<sup>12</sup>, S. Bernard<sup>12</sup>, P. Bernardi<sup>13</sup>, T. Bertrand<sup>13</sup>, O. Beyssac<sup>12</sup>, T. Bosak<sup>14</sup>, B. Bousquet<sup>15</sup>, A. Brown<sup>16</sup>, A. Cadu<sup>9</sup>, P. Caïs<sup>17</sup>, K. Castro<sup>8</sup>, B. Chide<sup>10</sup>, E. Clavé<sup>15</sup>, S. M. Clegg<sup>10</sup>, E. Cloutis<sup>7</sup>, S. Connell<sup>7</sup>, A. Cousin<sup>2</sup>, A. Debus<sup>18</sup>, E. Dehouck<sup>19</sup>, D. Delapp<sup>10</sup>, C. Donny<sup>18</sup>, A. Dorresoundiram<sup>13</sup>, G. Dromart<sup>19</sup>, B. Dubois<sup>20</sup>, C. Fabre<sup>21</sup>, A. Fau<sup>2</sup>, W. Fischer<sup>22</sup>, O. Forni<sup>2</sup>, T. Fouchet<sup>13</sup>, R. Francis<sup>23</sup>, J. Frydenvang<sup>24</sup>, T. Gabriel<sup>5</sup>, O. Gasnault<sup>2</sup>, E. Gibbons<sup>25</sup>, I. Gontijo<sup>23</sup>, X. Jacob<sup>26</sup>, J. R. Johnson<sup>27</sup>, H. Kalucha<sup>22</sup>, E. Kelly<sup>3</sup>, E. W. Knutsen<sup>28</sup>, G. Lacombe<sup>28</sup>, N. L. Lanza<sup>10</sup>, J. Laserna<sup>4</sup>, J. Lasue<sup>2</sup>, S. Le Mouélic<sup>29</sup>, C. Leggett IV<sup>10</sup>, R. Leveille<sup>25</sup>, E. Lewin<sup>11</sup>, G. Lopez-Reyes<sup>30</sup>, R. D. Lorenz<sup>27</sup>, E. Lorigny<sup>18</sup>, J. M. Madariaga<sup>8</sup>, M. Madsen<sup>24</sup>, S. Madsen<sup>23</sup>, L. Mandon<sup>13</sup>, N. Mangold<sup>29</sup>, M. Mann<sup>18</sup>, J.-A. Manrique<sup>10, 30</sup>, J. Martinez-Frias<sup>31</sup>, L. E. Mayhew<sup>32</sup>, T. McConnochie<sup>33</sup>, S. M. McLennan<sup>34</sup>, N. Melikechi<sup>35</sup>, P.-Y. Meslin<sup>2</sup>, F. Meunier<sup>18</sup>, D. Mimoun<sup>9</sup>, G. Montagnac<sup>19</sup>, F. Montmessin<sup>28</sup>, J. Moros<sup>4</sup>, V. Mousset<sup>18</sup>, N. Murdoch<sup>9</sup>, T. Nelson<sup>10</sup>, R. T. Newell<sup>10</sup>, A. Ollila<sup>10</sup>, Y. Parot<sup>2</sup>, P. Pilleri<sup>2</sup>, C. Pilorget<sup>36,37</sup>, P. Pinet<sup>2</sup>, G. Pont<sup>18</sup>, F. Poulet<sup>36</sup>, C. Quantin-Nataf<sup>19</sup>, B. Quertier<sup>17</sup>, W. Rapin<sup>2</sup>, A. Reyes-Newell<sup>10</sup>, S. Robinson<sup>10</sup>, L. Rochas<sup>18</sup>, C. Royer<sup>13</sup>, F. Rull<sup>30</sup>, V. Sautter<sup>12</sup>, S. Schröder<sup>38</sup>, S. Sharma<sup>3</sup>, V. Shridar<sup>23</sup>, A. Sournac<sup>9</sup>, A. Stott<sup>9</sup>, M. Toplis<sup>2</sup>, I. Torre-Fdez<sup>8</sup>, N. Turenne<sup>7</sup>, T. Tzanetos<sup>23</sup>, A. Udry<sup>39</sup>, M. Veneranda<sup>30</sup>, D. Venhaus<sup>10</sup>, D. Vogt<sup>38</sup> and P. Willis<sup>23</sup>

<sup>1</sup>Purdue University Earth, Atmospheric and Planetary Sciences department, West Lafayette, IN, USA.

<sup>2</sup>Institut de Recherche en Astrophysique et Planétologie, Université de Toulouse 3 Paul Sabatier, CNRS, CNES, Toulouse, France.

<sup>3</sup>University of Hawaii, Manoa, Hawaii, USA.

<sup>4</sup>Universidad de Malaga, Malaga, Spain.

<sup>5</sup>U.S. Geological Survey, Flagstaff, Arizona, USA.

<sup>6</sup>Department of Chemistry and Biochemistry, University of South Carolina, Columbia, South Carolina, USA.

<sup>7</sup>University of Winnipeg, Winnipeg, Canada.

<sup>8</sup>University of Basque Country, UPV/EHU, Leioa, Bilbao, Spain.

<sup>9</sup>Institut Supérieur de l'Aéronautique et de l'Espace (ISAE-SUPAERO), Université de Toulouse, Toulouse, France.

<sup>10</sup>Space and Planetary Exploration Team, Los Alamos National Laboratory, Los Alamos, New Mexico, USA.

<sup>11</sup>Institut de Planétologie et Astrophysique de Grenoble, CNRS, Univ. Grenoble Alpes, Grenoble, France.

- <sup>12</sup>Institut de Minéralogie, de Physique des Matériaux et de Cosmochimie, CNRS, Sorbonne Université, MNHN, Paris, France.
- <sup>13</sup>Laboratoire d'Etudes Spatiales et d'Instrumentation en Astrophysique, Obs. Paris, CNRS, Sorbonne Univ., Univ. Paris-Diderot, Meudon, France.
- <sup>14</sup>Earth, Atmospheric and Planetary Sciences, Massachusetts Institute of Technology, Cambridge, Massachusetts, USA.
- <sup>15</sup>Centre Lasers Intenses et Applications, CNRS, CEA, Univ. Bordeaux, Bordeaux, France.
- <sup>16</sup>Plancius Research, Severna Park, Maryland, USA.
- <sup>17</sup>Laboratoire d'Astrophysique de Bordeaux, CNRS, Univ. Bordeaux, Bordeaux, France.
- <sup>18</sup>Centre National d'Etudes Spatiales, Toulouse, France.
- <sup>19</sup>Univ. Lyon, UCBL, ENSL, UJM, CNRS, LGL-TPE, Villeurbanne, France.
- <sup>20</sup>Groupe d'Instrumentation Scientifique, Observatoire Midi-Pyrénées, Toulouse, France.
- <sup>21</sup>GéoRessources, CNRS, Univ. Lorraine, Nancy, France.
- <sup>22</sup>California Institute of Technology, Pasadena, California, USA.
- <sup>23</sup>Jet Propulsion Laboratory, California Institute of Technology, Pasadena, California, USA.
- <sup>24</sup>University of Copenhagen, Copenhagen, Denmark.
- <sup>25</sup>McGill University, Montreal, Canada.
- <sup>26</sup>Institut de Mécanique des Fluides, Univ. Toulouse 3 Paul Sabatier, INP, CNRS, Toulouse, France.
- <sup>27</sup>Space Exploration Sector, Johns Hopkins Applied Physics Laboratory, Laurel, Maryland, USA.
- <sup>28</sup>Laboratoire Atmosphères, Milieux, Observations Spatiales, CNRS, Univ. Saint-Quentin-en-Yvelines, Sorbonne Univ., Guyancourt, France.
- <sup>29</sup>Laboratoire Planétologie et Géosciences, CNRS, Université Nantes, Université Angers, Nantes, France.
- <sup>30</sup>University of Valladolid, Valladolid, Spain.
- <sup>31</sup>Agencia Estatal Consejo Superior de Investigaciones Científicas, Madrid, Spain.
- <sup>32</sup>Department of Geological Sciences, University of Colorado Boulder, Boulder, Colorado, USA.
- <sup>33</sup>University of Maryland, College Park, Maryland, USA.
- <sup>34</sup>State University of New York, Stony Brook, New York, USA.
- <sup>35</sup>Department of Physics and Applied Physics, Kennedy College of Sciences, University of Massachusetts, Massachusetts, USA.
- <sup>36</sup>Institut d'Astrophysique Spatiale, CNRS, Univ. Paris-Saclay, Orsay, France
- <sup>37</sup>Institut Universitaire de France, Paris, France.
- <sup>38</sup>Deutsches Zentrum für Luft- und Raumfahrt (DLR), Institute of Optical Sensor Systems, Berlin, Germany.
- <sup>39</sup>University of Nevada Las Vegas, Las Vegas, Nevada, USA.

### List of Abbreviations and Variables

Many abbreviations, acronyms and variables are used throughout the article. Their meaning is given in the tables below (Tables 3 and 4).

**Table 3**  
*List of Abbreviations and Acronyms*

AOTF	Acousto-optic tunable filter
Atm.	Atmosphere
BDNR	Band Depth to Noise Ratio
BG	Background (thermal)
DC	Dark current
Det.	Detector
DN	Digit Numbers (unit of raw digital data)
EMI/EMC	Electromagnetic Interference/Contamination
FM	Flight Model
FoV	Field of View
FS	Flight Spare
HK	Housekeeping (monitored variable to track the health of the instrument)
IRS	Infrared Spectrometer
ITF	Instrument Transfer Function
LIBS	Laser Induced Breakdown Spectroscopy
OBOX	Optical Box
PDS	Planetary Data System
QTH	Quartz-Tungsten-Halogen
RF	Radio Frequency
RON	Readout Noise
SCCT	SuperCam Calibration Target
SNR	Signal to Noise Ratio
TEC	Thermo-Electrical Cooler
TRLS	Time-Resolved Luminescence Spectroscopy
TRR	Time-Resolved Raman spectroscopy
VISIR	Visible and Near Infrared

**Table 4**  
*List of Recurring Variables*

Signal (capitalized)	Data collected when the AOTF is supplied with RF power
Dark (capitalized)	Data collected when the AOTF is not supplied with RF power
$t_{\text{int}}$	Integration time of the IRS
$P_{\text{RF}}$	RF power injected to the AOTF
$T_{\text{sp}}$	Temperature of the IRS optical box (spectrometer)
$T_{\text{ph}}$	Temperature of the detector (photodiode)
$T_{\text{board}}$	Temperature of the IRS electronic board

### List of SuperCam Data Products Used

#### White SCCT observations

SCAM\_0020\_0668712109\_057\_CP2\_scam01020\_SCCT\_IR\_White\_ \_ \_ \_ \_ \_ 01P31  
 SCAM\_0051\_0671463918\_837\_CP2\_scam01051\_SCCT\_IR\_White\_ \_ \_ \_ \_ \_ 01P31  
 SCAM\_0051\_0671463968\_835\_CP2\_scam01051\_SCCT\_IR\_White\_ \_ \_ \_ \_ \_ 01P31  
 SCAM\_0060\_0672274067\_291\_CP2\_scam02060\_SCCT\_IR\_White\_ \_ \_ \_ \_ \_ 01P31

SCAM_0072_0673327518_211_CP2_scam01072_SCCT_41_IRSAlign_ _ _ _ _	06P31
SCAM_0072_0673327699_186_CP2_scam01072_SCCT_41_IRSAlign_ _ _ _ _	07P31
SCAM_0072_0673327789_201_CP2_scam01072_SCCT_41_IRSAlign_ _ _ _ _	08P31
SCAM_0077_0673762222_750_CP2_scam03077_SCCT_IR_White_ _ _ _ _	01P31
SCAM_0111_0676799594_572_CP2_scam06111_SCCT_41_IRSAlign_ _ _ _ _	07P31
SCAM_0111_0676799673_536_CP2_scam06111_SCCT_41_IRSAlign_ _ _ _ _	08P31
SCAM_0112_0676881063_660_CP2_scam01112_SCCT_IR_White_ _ _ _ _	01P31
SCAM_0115_0677148349_703_CP2_scam03115_SCCT_IR_White_ _ _ _ _	01P31
SCAM_0115_0677148398_618_CP2_scam03115_SCCT_IR_White_ _ _ _ _	01P31
SCAM_0115_0677148448_591_CP2_scam03115_SCCT_IR_White_ _ _ _ _	01P31
SCAM_0115_0677148497_578_CP2_scam03115_SCCT_IR_White_ _ _ _ _	01P31
SCAM_0115_0677148547_557_CP2_scam03115_SCCT_IR_White_ _ _ _ _	01P31
SCAM_0115_0677149076_812_CP2_scam04115_SCCT_IR_White_ _ _ _ _	01P31
SCAM_0115_0677149125_810_CP2_scam04115_SCCT_IR_White_ _ _ _ _	01P31
SCAM_0115_0677149175_975_CP2_scam04115_SCCT_IR_White_ _ _ _ _	01P31
SCAM_0115_0677149224_790_CP2_scam04115_SCCT_IR_White_ _ _ _ _	01P31
SCAM_0115_0677149274_794_CP2_scam04115_SCCT_IR_White_ _ _ _ _	01P31
SCAM_0132_0678656329_412_CP2_scam04132_SCCT_IR_White_ _ _ _ _	01P31
SCAM_0154_0680613999_773_CP2_scam01154_SCCT_IR_White_ _ _ _ _	01P31
SCAM_0184_0683275592_792_CP2_scam06184_SCCT_IR_White_ _ _ _ _	01P31
SCAM_0201_0684781889_444_CP2_scam02201_SCCT_IR_White_ _ _ _ _	01P31
SCAM_0246_0688778799_499_CP2_scam03246_SCCT_IR_White_ _ _ _ _	01P31
SCAM_0265_0690459780_181_CP2_scam01265_SCCT_IR_White_ _ _ _ _	01P32
SCAM_0265_0690463801_324_CP2_scam04265_SCCT_IR_White_ _ _ _ _	01P31
SCAM_0274_0691262888_994_CP2_scam02274_SCCT_IR_White_ _ _ _ _	01P31
SCAM_0274_0691264507_788_CP2_scam04274_SCCT_IR_White_ _ _ _ _	01P31
SCAM_0286_0692327379_102_CP2_scam02286_SCCT_IR_White_ _ _ _ _	01P31
SCAM_0292_0692858939_216_CP2_scam02292_SCCT_IR_White_ _ _ _ _	01P31
SCAM_0294_0693036463_149_CP2_scam02294_SCCT_IR_White_ _ _ _ _	01P31
SCAM_0300_0693569438_583_CP2_scam03300_SCCT_IR_White_ _ _ _ _	01P31
SCAM_0304_0693923674_211_CP2_scam05304_SCCT_IR_White_ _ _ _ _	01P31
SCAM_0354_0698354602_742_CP2_scam01354_SCCT_IR_White_ _ _ _ _	01P31

**Color and mineral SCCTs**

SCAM_0011_0667917639_179_CP2_scam15207_SCCT_Black_ _ _ _ _	01P31
SCAM_0011_0667917951_977_CP2_scam15207_SCCT_Black_ _ _ _ _	01P31

SCAM_0077_0673773040_307_CP2_scam07077_SCCT_Cyan_	_____	05P31
SCAM_0077_0673773243_350_CP2_scam07077_SCCT_Red_	_____	03P31
SCAM_0077_0673773514_338_CP2_scam07077_SCCT_IR_black_	_____	02P31
SCAM_0079_0673951190_061_CP2_scam07079_SCCT_PMIIFS0505_	_____	10P31
SCAM_0079_0673952059_991_CP2_scam08079_SCCT_PMIEN0602_	_____	16P31
SCAM_0079_0673952246_960_CP2_scam08079_SCCT_PMIIDN0302_	_____	13P31
SCAM_0079_0673952427_993_CP2_scam08079_SCCT_PMIOR0507_	_____	12P31
SCAM_0246_0688778618_492_CP2_scam03246_SCCT_Cyan_	_____	05P31
<b>Other targets</b>		
SCAM_0147_0679986786_336_CP2_scam06147_LD_DistalCarbonates_	_____	09P31
SCAM_0357_0698618375_774_CP2_scam01357_Sky_357_	_____	03P32

### Conflict of Interest

The authors declare no conflicts of interest relevant to this study.

### Data Availability Statement

All the data supporting this study are either available on the NASA Planetary Data System (Maurice & Wiens, 2021) or on PSUP node (Royer, 2021).

### Acknowledgments

The authors are truly grateful for the SuperCam and Mars 2020 hardware operation teams for their investment in the mission. This work was supported by the CNES. Additional funding was provided by the following sources: NASA’s Mars exploration program, CNRS, IRIS OCAV, DIM ACAV, CSA, and the Natural Sciences and Research Council of Canada.

### References

Brown, A. J., Viviano, C. E., & Goudge, T. A. (2020). Olivine-carbonate mineralogy of the Jezero crater region. *Journal of Geophysical Research: Planets*, 125(3), e2019JE006011. <https://doi.org/10.1029/2019je006011>

Clave, E., Benzerara, K., Meslin, P. Y., Forni, O., Royer, C., Mandon, L., et al. (2022). Carbonate detection with SuperCam in igneous rocks on the floor of Jezero Crater, Mars. *Journal of Geophysical Research: Planets*, e2022JE007463. <https://doi.org/10.1029/2022JE007463>

Cousin, A., Sautter, V., Fabre, C., Dromart, G., Montagnac, G., Drouet, C., et al. (2022). SuperCam calibration targets on board the perseverance rover: Fabrication and quantitative characterization. *Spectrochimica Acta Part B: Atomic Spectroscopy*, 188, 106341. <https://doi.org/10.1016/j.sab.2021.106341>

Eigenbrode, J. L., Summons, R. E., Steele, A., Freissinet, C., Millan, M., Navarro-González, R., & Sutter, B. (2018). Organic matter preserved in 3-billion-year-old mudstones at Gale crater, Mars. *Science*, 360(6393), 1096–1101. <https://doi.org/10.1126/science.aas9185>

Farley, K. A., Stack, K. M., Shuster, D. L., Horgan, B. H. N., Hurowitz, J. A., Tarnas, J. D., et al. (2022). Aqueously altered igneous rocks sampled on the floor of Jezero crater, Mars. *Science*, 377(6614), eabo2196.

Farley, K. A., Williford, K. H., Stack, K. M., Bhartia, R., Chen, A., de la Torre, M., et al. (2020). Mars 2020 mission overview. *Space Science Reviews*, 216(8), 142. <https://doi.org/10.1007/s11214-020-00762-y>

Fassett, C. I., & Head, J. W., III. (2005). Fluvial sedimentary deposits on Mars: Ancient deltas in a crater lake in the Nili Fossae region. *Geophysical Research Letters*, 32, L14201. <https://doi.org/10.1029/2005GL023456>

Fouchet, T., Reess, J.-M., Montmessin, F., Hassen-Khodja, R., Nguyen-Tuong, N., Humeau, O., et al. (2022). The SuperCam infrared spectrometer for the perseverance rover of the Mars2020 mission. *Icarus*, 373, 114773. <https://doi.org/10.1016/j.icarus.2021.114773>

Goudge, T. A., Mustard, J. F., Head, J. W., Fassett, C. I., & Wiseman, S. M. (2015). Assessing the mineralogy of the watershed and fan deposits of the Jezero crater paleolake system, Mars. *Journal of Geophysical Research: Planets*, 120(4), 775–808. <https://doi.org/10.1002/2014je004782>

Grotzinger, J. P., Sumner, D. Y., Kah, L. C., Stack, K., Gupta, S., Edgar, L., et al. (2014). A habitable fluvio-lacustrine environment at Yellowknife Bay, Gale crater, Mars. *Science*, 343(6169), 1242777. <https://doi.org/10.1126/science.1242777>

Horgan, B. H. N., Anderson, R. B., Dromart, G., Amador, E. S., & Rice, M. S. (2020). The mineral diversity of Jezero crater: Evidence for possible lacustrine carbonates on Mars. *Icarus*, 339, 113526. <https://doi.org/10.1016/j.icarus.2019.113526>

Liu, Y., Tice, M. M., Schmidt, M. E., Treiman, A. H., Kizovski, T. V., Hurowitz, J. A., et al. (2022). An olivine cumulate outcrop on the floor of Jezero crater, Mars. *Science*, 377(6614), 1513–1519. <https://doi.org/10.1126/science.abo2756>

Mandon, L. (2020). *Préparation Des Futures Missions in Situ Martiennes via La Télédétection et l’expérimentation En Spectroscopie de Réflectance* (PhD thesis). Université de Lyon.

Mandon, L., Quantin-Nataf, C., Royer, C., Beck, P., Fouchet, T., Johnson, J. R., et al. (2022). Reflectance of Jezero crater floor: 2. Mineralogical interpretation. *Journal of Geophysical Research: Planets*, e2022JE007450. <https://doi.org/10.1029/2022JE007450>

Mangold, N., Gupta, S., Gasnault, O., Dromart, G., Tarnas, J. D., Sholes, S. F., et al. (2021). Perseverance rover reveals an ancient delta-lake system and flood deposits at Jezero crater, Mars. *Science*, 374(6568), 711–717. <https://doi.org/10.1126/science.aba14051>

Manrique, J. A., Lopez-Reyes, G., Cousin, A., Rull, F., Maurice, S., Wiens, R. C., et al. (2020). SuperCam calibration targets: Design and development. *Space Science Reviews*, 216(8), 138. <https://doi.org/10.1007/s11214-020-00764-w>



- Maurice, S., Wiens, R. C., Bernardi, P., Cais, P., Robinson, S., Nelson, T., et al. (2021). The SuperCam instrument suite on the Mars 2020 rover: Science objectives and mast-unit description. *Space Science Reviews*, 217(3), 47. <https://doi.org/10.1007/s11214-021-00807-w>
- Maurice, S. A., & Wiens, R. C. (2021). Mars 2020 SuperCam bundle. <https://doi.org/10.17189/1522646>
- Poulet, F., Royer, C., Beck, P., Mandon, L., Quantin-Nataf, C., Johnson, J. R., et al. (2022). Modal mineralogy of Séítah unit in Jezero Crater (Mars) retrieved from nonlinear unmixing analyses of IRS/SuperCam. *LPI Contribution*, 53, 2032.
- Royer, C. (2021). Infrared spectrometer onboard SuperCam/Mars 2020: Relationship between RF power and the optical transmission. <https://doi.org/10.48326/9db9-y054>
- Royer, C., Poulet, F., Reess, J.-M., Pilorget, C., Hamm, V., Fouchet, T., et al. (2020). Pre-launch radiometric calibration of the infrared spectrometer onboard SuperCam for the Mars2020 rover. *Review of Scientific Instruments*, 91(6), 063105. <https://doi.org/10.1063/1.5145390>
- Scheller, E. L., Razzell Hollis, J., Cardarelli, E. L., Steele, A., Beegle, L. W., Bhartia, R., et al. (2022b). First-results from the perseverance SHER-LOC investigation: Aqueous alteration processes and implications for organic geochemistry in Jezero Crater. *MARS*, 2678, 1652.
- Scheller, E. L., Razzell Hollis, J. R., Cardarelli, E. L., Steele, A., Beegle, L. W., Bhartia, R., et al. (2022a). Aqueous alteration processes in Jezero crater, Mars— implications for organic geochemistry. *Science*, eabo5204. <https://doi.org/10.1126/science.abo5204>
- Schon, S. C., Head, J. W., & Fassett, C. I. (2012). An overfilled lacustrine system and progradational delta in Jezero crater, Mars: Implications for Noachian climate. *Planetary and Space Science*, 67(1), 28–45. <https://doi.org/10.1016/j.pss.2012.02.003>
- Tice, M. M., Hurowitz, J. A., Allwood, A. C., Jones, M. W., Orenstein, B. J., Davidoff, S., et al. (2022). Alteration history of Séítah formation rocks inferred by PIXL X-ray fluorescence, X-ray diffraction, and multispectral imaging on Mars. *Science Advances*, 8(47), eabp9084. <https://doi.org/10.1126/sciadv.abp9084>
- Valle, S. (2017). *Design and application of high performance acousto-optic tunable filters* (PhD thesis). University of Glasgow.
- Viviano, C. E., Seelos, F. P., Murchie, S. L., Kahn, E. G., Seelos, K. D., Taylor, H. W., et al. (2014). Revised CRISM spectral parameters and summary products based on the currently detected mineral diversity on Mars. *Journal of Geophysical Research: Planets*, 119(6), 1403–1431. <https://doi.org/10.1002/2014je004627>
- Wiens, R. C., Maurice, S., Robinson, S. H., Nelson, A. E., Cais, P., Bernardi, P., et al. (2021). The SuperCam instrument suite on the NASA Mars 2020 rover: Body Unit and combined system tests. *Space Science Reviews*, 217(1), 4. <https://doi.org/10.1007/s11214-020-00777-5>
- Wiens, R. C., Udry, A., Beyssac, O., Quantin-Nataf, C., Mangold, N., Cousin, A., et al. (2022). Compositionally and density stratified igneous terrain in Jezero crater, Mars. *Science Advances*, 8(34), eabo3399.